

Chapter 14

Reconstruction Algorithms

The R Operator: From Field Maps to Source Inference

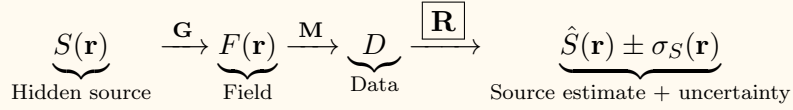
This chapter develops the **Reconstruction Operator \mathbf{R}** that maps measurement data D to source estimates $\hat{S}(\mathbf{r}) \pm \sigma_S(\mathbf{r})$. Without R , your system produces field maps (QFM). With R and uncertainty quantification, you achieve true **Quantum Field Imaging (QFI)**.

Connecting equation. The chapter culminates in the **QFI Imaging Figure of Merit:**

$$Q_{\text{IFOM}} = Q_{\text{FOM}} \times \Gamma_{\text{inv}} \times \Gamma_{\text{mm}}$$

where Q_{FOM} (Chapter 2) captures measurement throughput, $\Gamma_{\text{inv}} \in (0, 1]$ quantifies reconstruction fidelity, and $\Gamma_{\text{mm}} \in [0, 1]$ penalizes forward-model errors. Maximizing Q_{IFOM} —not just Q_{FOM} —is the design objective for any system aspiring to QFI status. This chapter develops the Reconstruction Operator \mathbf{R} , the final—and defining—stage of the QFI operator stack:

QFI Pipeline Position.



Abbreviated Terms

Table 14.1: Abbreviated terms used in this chapter

Abbreviation	Full Term
ADMM	Alternating Direction Method of Multipliers
CAD	Computer-Aided Design
CI	Confidence Interval
CRB	Cramér-Rao Bound
FIM	Fisher Information Matrix
GDSII	Graphic Design System II (IC layout format)
LASSO	Least Absolute Shrinkage and Selection Operator
MAP	Maximum A Posteriori
MLE	Maximum Likelihood Estimation
MSE	Mean Squared Error
NV	Nitrogen-Vacancy
ODMR	Optically Detected Magnetic Resonance
PSF	Point Spread Function
QFI	Quantum Field Imaging
QFM	Quantum Field Metrology
SNR	Signal-to-Noise Ratio
SVD	Singular Value Decomposition
TSVD	Truncated Singular Value Decomposition
TV	Total Variation
UQ	Uncertainty Quantification

Key Symbols and Operational Definitions

Symbol	Name	How to Measure / Compute
$S(r)$	Source distribution	Physical quantity to be reconstructed (e.g., current density $J(r)$ in A/m ²)
$\hat{S}(r)$	Source estimate	Output of reconstruction operator R applied to data D
$\sigma_S(r)$	Reconstruction uncertainty	Standard deviation of $\hat{S}(r)$ from analytical covariance or MC sampling
$A = M \cdot G$	System matrix	Product of measurement operator M (optics, sampling) and source-to-field operator G (Biot-Savart, thermal)
$\kappa(A)$	Condition number	$\sigma_{\max}(A)/\sigma_{\min}(A)$; compute via SVD or estimate from iterative solver
\mathbf{J}	Fisher Information Matrix	$\mathbf{J} = A^T \Sigma^{-1} A$ for Gaussian noise; compute from forward model and noise covariance
Γ_{inv}	Reconstruction fidelity	$\text{tr}(\mathbf{J}^{-1})/\text{tr}(\text{Cov}(\hat{S}))$; measures efficiency vs. CRB floor
Γ_{mm}	Model-mismatch penalty	Product of residual, cross-prediction, and whiteness scores (Eq. 14.35); computed <i>after</i> reconstruction
Q_{FOM}	Measurement throughput	From Chapter 2: $\eta_q \times N_{\parallel} \times \Phi_{\text{multi}}/t_{\text{acq}}$
Q_{IFOM}	Imaging figure of merit	$Q_{\text{FOM}} \times \Gamma_{\text{inv}} \times \Gamma_{\text{mm}}$; the complete system-level QFI performance metric
ρ	Normalized residual	$\ D - A\hat{S}\ /\sqrt{m\sigma_n^2}$; should be ≈ 1 for valid reconstruction

Abstract

This chapter develops the reconstruction operator \mathbf{R} that converts quantum-field measurements D into source estimates $\hat{S}(\mathbf{r}) \pm \sigma_S(\mathbf{r})$. We formulate the QFI inverse problem $D = \mathbf{A}S + \epsilon$ with $\mathbf{A} = \mathbf{M} \cdot \mathbf{G}$, explain ill-posedness, and use conditioning to connect standoff distance, sensor geometry, and reconstruction stability. A core regularization toolkit—Tikhonov (ℓ_2), Total Variation, and ℓ_1 /LASSO—is presented together with a decision flowchart for method and λ selection. For photon-starved or nonnegative regimes, we add Richardson–Lucy (RL) and RL-TV deconvolution, and we extend to semi-blind and physics-aware blind reconstruction when the forward kernel (e.g., standoff, PSF, drift) is uncertain.

Fundamental limits are derived via Fisher information and the Cramér–Rao bound (CRB), leading to the reconstruction fidelity factor $\Gamma_{\text{inv}} = \text{CRB}/\text{MSE}_{\text{achieved}}$. Reconstruction quality is integrated into the system metric

$$Q_{\text{IFOM}} = Q_{\text{FOM}} \times \Gamma_{\text{inv}} \times \Gamma_{\text{mm}},$$

where Γ_{mm} is a residual- and cross-physics-based model-mismatch penalty that provides a go/no-go criterion for trusting reconstructions. We show how CAD-informed priors and multi-physics correlation reduce effective condition numbers, how iterative solvers (ADMM, proximal methods, acceleration) make large-scale 3D inversion practical, and how Bayesian inference yields posterior uncertainty—including sampling-based estimates beyond the Gaussian-linear case.

Complete worked examples demonstrate end-to-end current-density imaging from wide-field NV magnetic maps with per-voxel confidence intervals and falsification tests.

14.1 Introduction: Why Reconstruction Completes QFI

14.1.1 Historical Context

The history of scientific imaging is fundamentally a history of inverse problems. From Roentgen's first X-ray images to modern MRI, every imaging modality faces the same challenge: inferring hidden structure from indirect measurements. The transition from measurement to imaging always requires solving an inverse problem.

In the context of Quantum Field Imaging (QFI), this chapter addresses the critical transition from Quantum Field Metrology (QFM) to true QFI. While earlier chapters developed the physics of quantum sensing and optical systems, this chapter provides the mathematical machinery to transform raw measurements into actionable source estimates.

Key historical milestones:

- **1895:** Roentgen's X-rays — direct projection imaging
- **1917:** Radon transform — mathematical foundation for tomography
- **1963:** Tikhonov regularization — stable inversion of ill-posed problems
- **1973:** CT scanner (Hounsfield) — practical inverse problem solution
- **2003:** Compressed sensing (Candès, Tao) — sparse reconstruction
- **2020s:** NV-based magnetic microscopy — QFI emergence

14.1.2 Pain Points in Current Practice

Chapters 10–11 constructed the forward model \mathbf{G} that maps source distributions to physical fields; Chapters 3–9 and 12 developed the measurement operator \mathbf{M} that converts fields to discrete data. This chapter addresses the central question: *how do we invert the cascade $\mathbf{M} \cdot \mathbf{G}$ to recover the source $S(\mathbf{r})$ from noisy data D ?*

Without the reconstruction operator \mathbf{R} , a quantum sensor system delivers only calibrated field maps—Quantum Field Metrology (QFM). It is \mathbf{R} , together with uncertainty quantification, that promotes QFM to true **Quantum Field Imaging (QFI)**. The two-layer taxonomy introduced in Chapter 1 is realized here in its most concrete form: \mathbf{R} transforms photon-count data into a three-dimensional current-density estimate $\hat{\mathbf{J}}(\mathbf{r})$ with per-voxel confidence intervals, enabling engineers to answer “*where is the defect and how confident are we?*”—a question that field maps alone cannot address.

Actually, current quantum sensing systems face several critical challenges that prevent their transition from QFM to QFI:

1. **Ill-posedness:** The inverse problem $B(r) \rightarrow J(r)$ is severely ill-conditioned, with condition numbers $\kappa > 10^6$ typical for deep sources
2. **Lack of uncertainty quantification:** Most systems report point estimates without confidence bounds, making engineering decisions unreliable
3. **Model-measurement mismatch:** Forward model errors ($\Gamma_{mm} < 1$) degrade reconstruction fidelity
4. **Computational cost:** Full 3D reconstruction for large-scale ICs requires efficient algorithms

Hence, this chapter provides:

1. The **inverse-problem formulation** that casts QFI reconstruction as a regularized optimization problem (Section 14.2);
2. A **toolkit of regularization methods**—Tikhonov (ℓ_2), Total Variation, and ℓ_1 /LASSO— together with a practical decision flowchart for method and λ selection (Section 14.3);
3. **Richardson–Lucy deconvolution** and **blind/semi-blind** inversion when the measurement statistics are Poisson or when the forward kernel (e.g., standoff) is uncertain (Section 14.4);
4. The **Cramér–Rao Bound (CRB)** and Fisher Information Matrix that set the fundamental accuracy floor, including how multi-physics channels increase information and tighten the CRB (Section 14.5);
5. The **reconstruction fidelity metric** Γ_{inv} and actionable design proxies for improving it under real SNR and conditioning constraints (Section 14.6);
6. **CAD-informed priors** that exploit IC design knowledge to reduce condition numbers by 3–10× and boost yield in production settings (Section 14.7);
7. **Uncertainty quantification** for source estimates $\hat{S}(\mathbf{r}) \pm \sigma_S(\mathbf{r})$ via both analytical propagation and Monte Carlo validation (Section 14.8);
8. **Residual analysis and falsification testing** that define the operational model-mismatch penalty Γ_{mm} and provide go/no-go criteria for trusting reconstruction results (Section 14.9);
9. **Iterative solvers** (ADMM, proximal gradient, acceleration) that make large-scale 3D reconstructions computationally feasible (Section 14.10);
10. The **Bayesian reconstruction framework** (posterior, MAP, and sampling) for principled fusion of priors and data, and for uncertainty beyond the Gaussian-linear case (Section 14.11);
11. **Complete worked examples** that walk through the full QFI pipeline end-to-end (Section 14.12).

14.1.3 Figures of Merit for Reconstruction

This chapter introduces two key metrics for QFI reconstruction quality:

The reconstruction fidelity factor measures how close the achieved reconstruction approaches the fundamental limit:

$$\Gamma_{\text{inv}} = \frac{\text{CRB}}{\text{MSE}_{\text{achieved}}} = \frac{\text{Fundamental limit}}{\text{Achieved error}} \quad (14.1)$$

where $\Gamma_{\text{inv}} \in (0, 1]$, with $\Gamma_{\text{inv}} = 1$ indicating optimal reconstruction.

The complete QFI imaging figure of merit combines measurement throughput with reconstruction quality:

$$Q_{\text{IFOM}} = Q_{\text{FOM}} \times \Gamma_{\text{inv}} \times \Gamma_{\text{mm}} \quad (14.2)$$

where Q_{FOM} is the measurement throughput (from Chapter 2), Γ_{inv} is reconstruction fidelity, and Γ_{mm} is the model-mismatch penalty.

The three factors in the Q_{IFOM} equation have distinct roles:

- Q_{FOM} (from Chapter 2): measurement throughput combining quantum sensitivity, parallelism, and multi-physics correlation.
- $\Gamma_{\text{inv}} \in (0, 1]$: reconstruction fidelity, measuring how close the achieved reconstruction variance approaches the Cramér–Rao bound (Section 14.5).
- $\Gamma_{\text{mm}} \in [0, 1]$: **model-mismatch penalty**, quantifying the trustworthiness of the forward model used in reconstruction. $\Gamma_{\text{mm}} = 1$ indicates perfect model–data agreement; $\Gamma_{\text{mm}} = 0$ indicates reconstruction failure due to model inadequacy (Section 14.8).

Critically, Γ_{mm} is not a design parameter but a **measured diagnostic**: it is computed from residual statistics and cross-physics prediction tests *after* reconstruction. Its operational definition is developed in Section 14.8.2.

14.1.4 Chapter Roadmap

This chapter proceeds as follows:

1. **Section 14.2:** Mathematical formulation of the QFI inverse problem
2. **Section 14.3:** Regularization methods (Tikhonov, TV, ℓ_1) and practical λ selection
3. **Section 14.4:** Richardson–Lucy deconvolution and blind/semi-blind reconstruction under Poisson noise and kernel uncertainty
4. **Section 14.5:** Cramér–Rao bound and Fisher information for QFI
5. **Section 14.6:** Strategies for optimizing reconstruction fidelity Γ_{inv}
6. **Section 14.7:** CAD-informed reconstruction for IC applications
7. **Section 14.8:** Uncertainty quantification for $\hat{S}(\mathbf{r}) \pm \sigma_S(\mathbf{r})$
8. **Section 14.9:** Residual analysis and falsification testing (including the operational definition of Γ_{mm})
9. **Section 14.10:** Iterative algorithms (ADMM, proximal gradient, acceleration)
10. **Section 14.11:** Bayesian reconstruction framework (MAP, posterior uncertainty, and sampling)
11. **Section 14.12:** Complete worked examples of the end-to-end QFI reconstruction pipeline

14.2 The QFI Inverse Problem

14.2.1 From Operator Stack to Reconstruction

Recall the QFI operator stack from Chapter 1:

$$S(r) \xrightarrow{G} F(r) \xrightarrow{M} D \xrightarrow{R} \hat{S}(r) \pm \sigma_S(r) \quad (14.3)$$

Remark 14.2.1 (Special Case: $S(r)$ vs. $J(r)$). Throughout this chapter, $S(r)$ denotes the generic source distribution to be reconstructed. In the specific QFI application of current-density imaging, $S(r) \equiv J(r)$ (current density vector field). In multi-physics contexts, $S(r)$ may also include thermal source terms (power dissipation) or strain fields. The operator stack notation $S \rightarrow G \rightarrow F \rightarrow M \rightarrow D \rightarrow R \rightarrow \hat{S}$ uses S as the generic source throughout for consistency with Chapter 1.

The reconstruction operator R must invert the cascade $M \circ G$ from discrete noisy measurements D to estimate the continuous source distribution $S(r)$.

Definition 14.2.1 (QFI Inverse Problem). Given measurement data $D \in \mathbb{R}^m$ related to source parameters $S \in \mathbb{R}^n$ through:

$$D = M \cdot G \cdot S + \epsilon, \quad \epsilon \sim \mathcal{N}(0, \Sigma) \quad (14.4)$$

the **QFI inverse problem** is to find \hat{S} that best explains D while respecting prior knowledge about S .

14.2.2 Ill-Posedness and Why It Matters

The QFI inverse problem is *ill-posed* in the sense of Hadamard: small perturbations in data D can lead to arbitrarily large changes in the solution \hat{S} . This ill-posedness arises from the physics of field propagation.

Figure 14.1 illustrates the fundamental challenges of ill-posed inverse problems in QFI, showing singular value decay, noise amplification, and the effect of standoff distance on condition number.

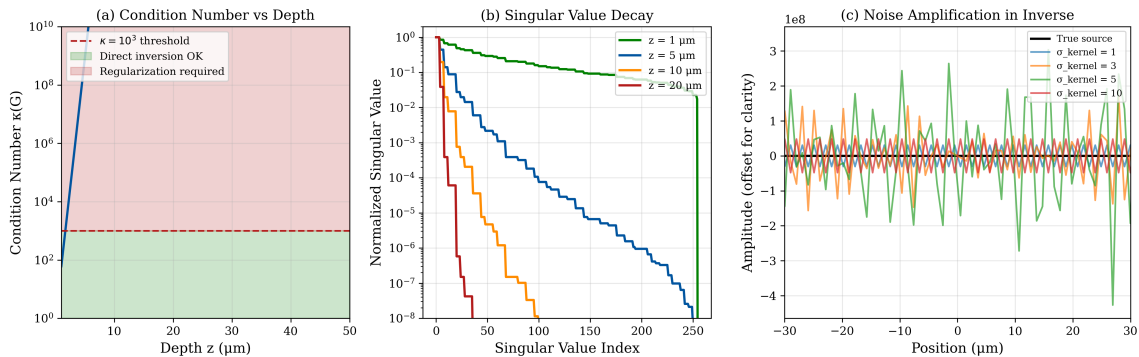


Figure 14.1: Ill-posedness of the QFI inverse problem. (a) Singular value spectrum of the Biot-Savart operator showing exponential decay with spatial frequency. (b) Noise amplification in naive inversion demonstrating the need for regularization. (c) Condition number scaling with standoff distance, showing $\kappa \propto e^{k_{\max} z}$ behavior. (d) Comparison of true source vs. unregularized reconstruction, illustrating severe noise amplification without proper regularization.

Theorem 14.2.1 (Condition Number Scaling). *For the 2D Biot-Savart forward model mapping current density $J(x, y)$ to magnetic field $B_z(x, y)$ at standoff z , the condition number scales as:*

$$\kappa(\mathbf{G}) \sim e^{k_{\max} z} \quad (14.5)$$

where $k_{\max} = \pi/\Delta x$ is the maximum spatial frequency determined by the discretization grid spacing Δx .

Assumptions for Condition Number Scaling (Eq. 14.5)

The condition number scaling $\kappa(G) \sim e^{k_{\max} z}$ in Theorem 14.2.1 is derived under the following assumptions:

- (a) **DFT-grid approximation:** The source and measurement planes are discretized on a uniform grid with spacing Δx , giving $k_{\max} = \pi/\Delta x$. Boundary effects are neglected (periodic or large-field approximation).
- (b) **Scalar field:** Only the B_z component of the magnetic field is considered. Full vector (B_x, B_y, B_z) reconstruction changes the singular value structure and generally *improves* conditioning.
- (c) **No sensor point spread function (PSF):** The sensor is treated as a point sampler. In practice, the optical PSF and pixel integration act as a low-pass filter that attenuates high- k components *before* inversion, reducing the effective k_{\max} .
- (d) **k_{\min} neglected:** The minimum spatial frequency $k_{\min} = 2\pi/L_{\text{FOV}}$ set by the field of view is assumed negligible relative to k_{\max} . For small FOV systems, k_{\min} contributes to the condition number through the ratio k_{\max}/k_{\min} .

Practical design quantity. In a real QFI instrument, we invert not G alone but the *combined system matrix*:

$$A = M \cdot G, \quad (14.6)$$

where M incorporates the optical PSF, pixel integration, spatial sampling, and any pre-processing filters (Chapter 8). The practical design target is therefore $\kappa(A)$, not $\kappa(G)$:

$$\kappa_{\text{eff}} \equiv \kappa(A) = \kappa(M \cdot G) \leq \kappa(M) \kappa(G). \quad (14.7)$$

Because M acts as a bandwidth-limiting operator, it truncates the high- k singular values of G that drive ill-conditioning, so that typically $\kappa(A) \ll \kappa(G)$. This makes **optical system design an implicit regularizer**: the MTF cutoff of the imaging optics (Chapters 5–8) directly controls the effective condition number available to the reconstruction algorithm.

Consequence for co-design. Equation (14.7) establishes that optical design and reconstruction algorithm selection are *coupled* design variables. Optimizing the Q-OTF (Chapter 7) to maximize spatial bandwidth while maintaining $\kappa(A) < 10^4$ (Design Rule 14.2.1) is the joint optical–reconstruction design target for QFI systems.

Proof. In Fourier space, the Biot-Savart kernel is $\tilde{G}(k) = \frac{\mu_0}{2} e^{-|k|z}$. The condition number is the ratio of maximum to minimum singular values:

$$\kappa(\mathbf{G}) = \frac{\sigma_{\max}}{\sigma_{\min}} = \frac{e^{-k_{\min} z}}{e^{-k_{\max} z}} = e^{(k_{\max} - k_{\min})z} \quad (14.8)$$

For typical discretizations where $k_{\min} \ll k_{\max}$, this reduces to $\kappa(\mathbf{G}) \sim e^{k_{\max} z}$. □

For stable reconstruction with condition number $\kappa < 10^4$, the standoff distance z must satisfy:

$$z < \frac{\ln(10^4)}{k_{\max}} \approx \frac{9.2\Delta x}{\pi} \approx 3\Delta x \quad (14.9)$$

To resolve 1 μm features, the standoff must be $z < 3 \mu\text{m}$.

14.2.3 Discretization Strategy

For computational implementation, we discretize the source volume into n voxels:

$$S(r) \approx \sum_{j=1}^n s_j \phi_j(r) \quad (14.10)$$

where $\phi_j(r)$ are basis functions (typically indicator functions for voxel grids).

The forward model becomes a matrix equation:

$$\mathbf{d} = \mathbf{A}\mathbf{s} + \boldsymbol{\epsilon} \quad (14.11)$$

where $\mathbf{A} = \mathbf{M} \cdot \mathbf{G}$ is the $m \times n$ system matrix.

14.3 Regularization Methods

Regularization stabilizes the ill-posed inverse problem by incorporating prior knowledge about the source. The general regularized reconstruction takes the form:

The general form of regularized reconstruction is:

$$\hat{S} = \underset{S}{\operatorname{argmin}} \left\{ \|D - \mathbf{A}S\|_2^2 + \lambda \mathcal{R}(S) \right\} \quad (14.12)$$

where $\mathcal{R}(S)$ is the regularization functional and $\lambda > 0$ is the regularization parameter controlling the data-fidelity vs. smoothness tradeoff.

14.3.1 Tikhonov Regularization (ℓ_2)

The simplest and most common regularization penalizes solution energy:

$$\mathcal{R}_{\text{Tik}}(S) = \|LS\|_2^2 \quad (14.13)$$

where L is a regularization matrix (identity for standard Tikhonov, derivative operators for smoothness constraints).

Theorem 14.3.1 (Tikhonov Solution). *The Tikhonov-regularized solution has closed form:*

$$\hat{S}_{\text{Tik}} = (\mathbf{A}^T \mathbf{A} + \lambda L^T L)^{-1} \mathbf{A}^T D \quad (14.14)$$

Properties: Tikhonov regularization smooths the solution, suppressing high-frequency oscillations. It biases the solution toward zero (or prior mean) and is analytically tractable with predictable behavior. Typical reconstruction fidelity: $\Gamma_{\text{inv}} \approx 0.75\text{--}0.85$ for QFI scenarios.

14.3.1.1 Reconstruction Transfer Function $H_R(k)$ and Connection to Q-OTF

When the forward operator is (approximately) shift-invariant, the measurement model can be written in the Fourier domain as

$$D(k) = H(k) S(k) + N(k), \quad (14.15)$$

where $H(k)$ is the *measurement transfer function* implied by the QFI operator $\mathbf{A} = \mathbf{M} \cdot \mathbf{G}$ and $N(k)$ is measurement noise. In this setting, many regularized reconstructions are linear filters of the form

$$\hat{S}(k) = R(k) D(k). \quad (14.16)$$

We define the **reconstruction transfer function**

$$H_R(k) \equiv R(k) H(k), \quad (14.17)$$

which plays the same interpretive role for reconstruction that the OTF/MTF plays for direct imaging: it quantifies which spatial frequencies are faithfully transmitted to the reconstructed source estimate. For Tikhonov regularization with a quadratic penalty, the Fourier-domain filter is

$$R_{\text{Tik}}(k) = \frac{H^*(k)}{|H(k)|^2 + \lambda|L(k)|^2}, \quad \Rightarrow \quad H_R(k) = \frac{|H(k)|^2}{|H(k)|^2 + \lambda|L(k)|^2}, \quad (14.18)$$

so $0 \leq H_R(k) \leq 1$ with a smooth roll-off controlled by λ . A convenient passband definition is the “half-power” cutoff k^* where $H_R(k^*) = 1/2$, which directly ties the regularization strength to a spatial resolution target [14.1, 14.2].

In QFI, $H(k)$ is not purely optical; it is a *quantum measurement transfer* that depends on the sensor physics (e.g., NV response, standoff, and readout sequence) and on the chosen observation channel(s). For this reason, it is useful to view the QFI pipeline as **Q-OTF → reconstruction filter**: the measurement stage determines $H(k)$ (a Q-OTF analogue), while regularization shapes $H_R(k)$ to trade bias for variance. Sections 14.5–14.6 then connect this spectral picture to fundamental limits (CRB) and to the achieved fidelity metric Γ_{inv} .

14.3.2 Total Variation Regularization

For sources with sharp edges (e.g., current pathways in ICs), Total Variation [14.3] preserves discontinuities:

$$\mathcal{R}_{\text{TV}}(S) = \int |\nabla S(r)| dr \approx \sum_i |(\nabla S)_i| \quad (14.19)$$

Total Variation preserves edges while smoothing flat regions, making it excellent for IC current reconstruction where conductors have sharp boundaries. Typical reconstruction fidelity: $\Gamma_{\text{inv}} \approx 0.80\text{--}0.90$ for sparse/edge sources.

14.3.3 ℓ_1 Regularization (LASSO)

For sparse sources (isolated defects), ℓ_1 promotes sparsity [14.4, 14.19, 14.20]:

$$\mathcal{R}_{\ell_1}(S) = \|S\|_1 = \sum_i |s_i| \quad (14.20)$$

Theorem 14.3.2 (Sparse Recovery Guarantee). *If source S has at most k non-zero components and measurement matrix \mathbf{A} satisfies the Restricted Isometry Property (RIP) with constant $\delta_{2k} < \sqrt{2} - 1$, then ℓ_1 minimization recovers S exactly from noiseless measurements $D = \mathbf{AS}$.*

Figure 14.2 compares the three regularization approaches on a test problem with mixed sparse and smooth source components.

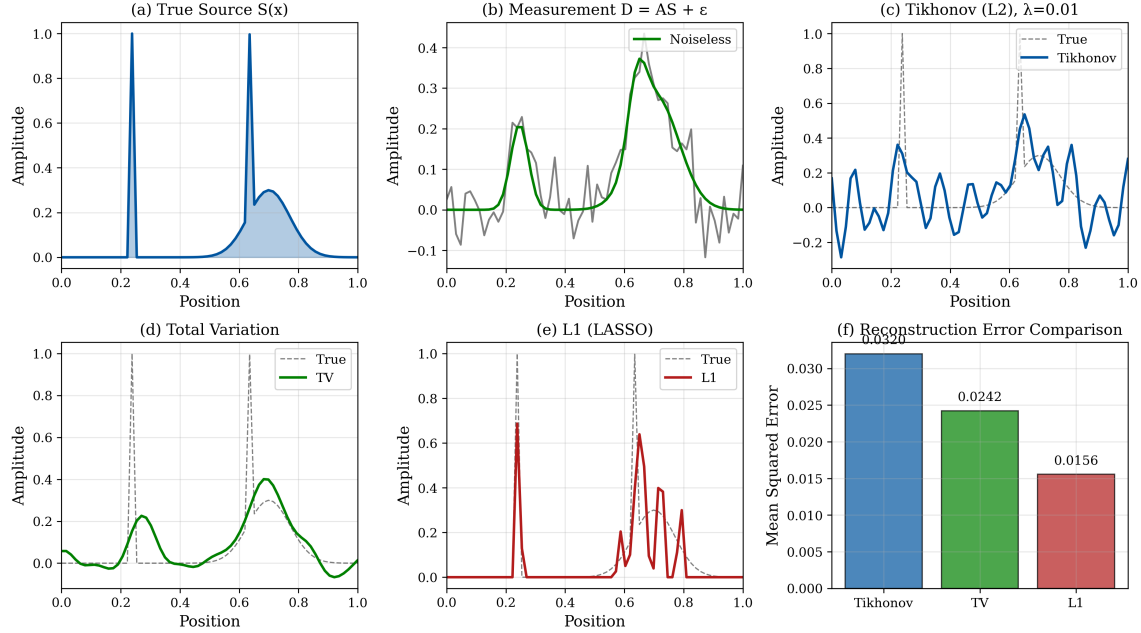


Figure 14.2: Comparison of regularization methods for QFI reconstruction. (a) True source distribution with sparse spikes and smooth background. (b) Noisy measurement data. (c) Tikhonov reconstruction showing smoothing of both spikes and background. (d) Total Variation reconstruction preserving edges but with staircase artifacts. (e) ℓ_1 reconstruction recovering sparse components accurately. (f) Mean squared error comparison demonstrating optimal method selection depends on source characteristics.

14.3.4 Regularization Parameter Selection

The parameter λ controls the bias-variance tradeoff. The L-curve method [14.15] provides a practical approach to parameter selection by plotting the solution norm against the residual norm.

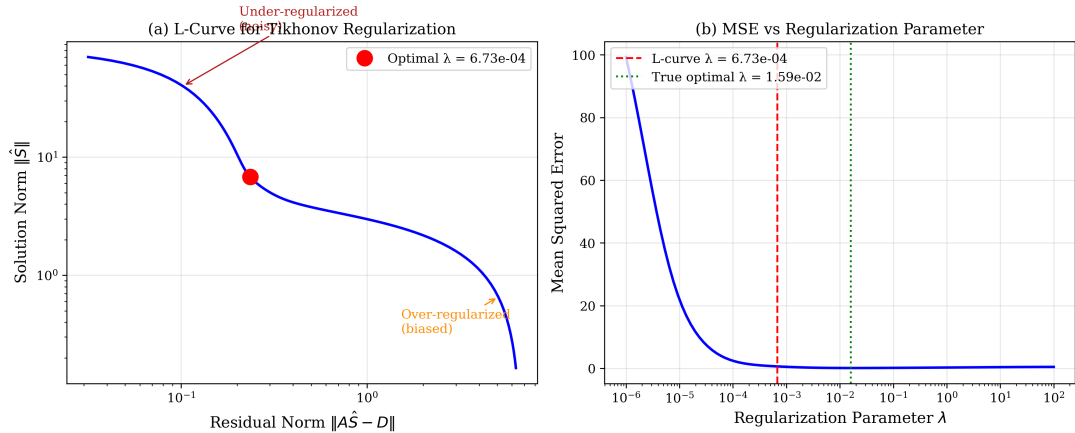


Figure 14.3: L-curve method for regularization parameter selection. (a) The characteristic L-shaped curve plotting solution norm $\|\hat{S}\|$ vs. residual norm $\|D - \mathbf{A}\hat{S}\|$. The corner point (marked in red) indicates optimal regularization. Under-regularized solutions (lower-left) are noisy; over-regularized solutions (upper-right) are biased. (b) Mean squared error vs. regularization parameter showing the L-curve selection closely approximates the true optimal.

For QFI systems with known measurement noise σ , use the discrepancy principle: select λ such that $\|D - \mathbf{A}\hat{S}\|_2 \approx \sqrt{m}\sigma$. For unknown noise, use GCV with 5-fold cross-validation.

Table 14.2: Recommended regularization strength by problem regime. The κ and SNR columns indicate the regime where each λ range is typical.

Regime	λ/λ_{\max}	Γ_{inv}	Range	Typical κ	Typical SNR
Well-posed	10^{-6} – 10^{-4}	0.90	–0.98	$< 10^2$	> 100
Mildly ill-posed	10^{-4} – 10^{-2}	0.70	–0.90	10^2 – 10^3	30–100
Moderately ill-posed	10^{-2} – 10^{-1}	0.40	–0.70	10^3 – 10^4	10–30
Severely ill-posed	10^{-1} – 10^0	< 0.40		$> 10^4$	< 10

14.4 Richardson-Lucy and Blind Deconvolution

The regularization methods of Section 14.3 assume that the forward operator \mathbf{A} is known exactly. In practice, the QFI forward model $\mathbf{A} = \mathbf{M} \cdot \mathbf{G}$ contains uncertainties arising from imprecise standoff distance calibration, inhomogeneous NV layer thickness, and optical PSF variations across the field of view. This section develops two complementary approaches that address these realities: Richardson-Lucy (RL) deconvolution, which naturally handles Poisson photon-counting statistics; and blind/semi-blind deconvolution, which jointly estimates the source and the uncertain kernel.

14.4.1 Historical Context and Motivation

Richardson-Lucy deconvolution originated independently in the work of W. H. Richardson (1972) [14.9] in the context of satellite image restoration and L. B. Lucy (1974) [14.10] for stellar photometry. The algorithm gained prominence in the astronomical community following the Hubble Space Telescope's spherical aberration correction, where RL deconvolution was used

to recover near-diffraction-limited images from severely aberrated data prior to the COSTAR corrective optics installation [14.12].

In microscopy, RL deconvolution became the standard for fluorescence image restoration, particularly in confocal and wide-field modalities where photon-counting statistics dominate the noise model [14.2]. The algorithm’s natural compatibility with Poisson noise—the dominant noise source in NV fluorescence imaging—makes it a compelling candidate for QFI reconstruction.

Why RL matters for QFI. The NV-based QFI measurement pipeline ultimately produces photon counts from sCMOS or EMCCD detectors. While the ODMR spectral fitting stage (Section 14.1) converts raw photon counts into frequency-shift maps $\Delta\nu(x, y)$, and hence into field estimates $B_z(x, y)$, the underlying noise statistics of these maps inherit Poisson characteristics modulated by the fitting process. In the high-count regime ($N_{\text{photon}} \gg 1$), Gaussian approximations are adequate and the ℓ_2 -based methods of Section 14.3 perform well. However, in the photon-starved regime—relevant for high-speed imaging or single-NV measurements—the Poisson-native RL algorithm provides superior performance by respecting the true noise model.

Furthermore, RL deconvolution enforces non-negativity of the reconstructed source, which is physically meaningful: current magnitudes $|\mathbf{J}|$ and thermal power densities Q are inherently non-negative quantities. The ℓ_2 and ℓ_1 methods of Section 14.3 do not guarantee non-negativity without additional constraints.

14.4.2 Richardson-Lucy Algorithm: Derivation from Poisson MLE

We derive the RL update rule from first principles as the Expectation-Maximization (EM) algorithm applied to Poisson likelihood maximization.

14.4.2.1 Poisson Observation Model

In the photon-counting regime, each measurement pixel d_i follows a Poisson distribution:

$$p(d_i | S) = \frac{(\mathbf{AS})_i^{d_i} e^{-(\mathbf{AS})_i}}{d_i!} \quad (14.21)$$

where $(\mathbf{AS})_i = \sum_j A_{ij} S_j$ is the expected count at pixel i . The full log-likelihood for independent pixels is:

$$\ln \mathcal{L}(S) = \sum_{i=1}^m [d_i \ln(\mathbf{AS})_i - (\mathbf{AS})_i - \ln(d_i!)] \quad (14.22)$$

Maximizing $\ln \mathcal{L}$ over $S \geq 0$ directly is intractable due to the logarithm of a sum. The EM algorithm introduces “complete data” to produce an iterative scheme with guaranteed monotonic likelihood increase.

14.4.2.2 EM Derivation of the RL Update

E-step: Define the “complete data” as the individual contributions n_{ij} of source voxel j to measurement pixel i :

$$\mathbb{E}[n_{ij} | d_i, S^{(k)}] = d_i \frac{A_{ij} S_j^{(k)}}{(\mathbf{AS}^{(k)})_i} \quad (14.23)$$

M-step: Maximize the expected complete-data log-likelihood with respect to S_j :

$$S_j^{(k+1)} = \frac{S_j^{(k)}}{\sum_i A_{ij}} \sum_{i=1}^m A_{ij} \frac{d_i}{(\mathbf{AS}^{(k)})_i} \quad (14.24)$$

Recognizing $\sum_i A_{ij}$ as the column sum of the system matrix (the “sensitivity” or “normalization” of voxel j), we arrive at the Richardson-Lucy update in compact matrix notation:

$$S^{(k+1)} = \frac{S^{(k)}}{\mathbf{A}^T \mathbf{1}} \cdot \mathbf{A}^T \left(\frac{D}{\mathbf{A} S^{(k)}} \right) \quad (14.25)$$

where all operations (multiplication, division) are element-wise.

Theorem 14.4.1 (RL Convergence Properties). *The Richardson-Lucy iteration (14.25) satisfies:*

1. **Monotonic likelihood increase:** $\ln \mathcal{L}(S^{(k+1)}) \geq \ln \mathcal{L}(S^{(k)})$, with equality only at a stationary point.
2. **Non-negativity preservation:** If $S^{(0)} > 0$ (component-wise), then $S^{(k)} > 0$ for all k .
3. **Flux conservation:** $\sum_j S_j^{(k+1)} = \sum_j S_j^{(k)}$ when \mathbf{A} is column-normalized ($\sum_i A_{ij} = 1$ for all j).

Proof. (1) **Monotonicity:** Follows directly from the EM algorithm's general convergence theorem: the M-step maximizes the surrogate function $Q(S|S^{(k)})$, which lower-bounds $\ln \mathcal{L}(S)$ by Jensen's inequality.

(2) **Non-negativity:** By inspection of Eq. (14.25), $S^{(k+1)}$ is a product of non-negative terms: $S^{(k)} > 0$, $A_{ij} \geq 0$, $d_i \geq 0$, and $(\mathbf{A} S^{(k)})_i > 0$ (given $S^{(k)} > 0$).

(3) **Flux conservation:** Summing Eq. (14.24) over j and using $\sum_j A_{ij} = 1$ (for a normalized PSF) gives $\sum_j S_j^{(k+1)} = \sum_i d_i$, which is constant. \square

Remark 14.4.1 (Semi-convergence and Early Stopping). While RL iterations monotonically increase the Poisson likelihood, the reconstruction quality (measured by MSE to the true source) typically exhibits **semi-convergence**: MSE decreases initially, reaches a minimum at iteration k^* , then increases as the algorithm begins fitting noise. This is analogous to the regularization parameter λ in Tikhonov: the iteration count k acts as an implicit regularization parameter, with $1/k$ playing the role of λ .

For QFI applications, use the discrepancy principle to select k^* : stop when the Poisson deviance

$$\mathcal{D}^{(k)} = 2 \sum_{i=1}^m \left[d_i \ln \frac{d_i}{(\mathbf{A} S^{(k)})_i} - d_i + (\mathbf{A} S^{(k)})_i \right] \quad (14.26)$$

satisfies $\mathcal{D}^{(k^*)} \approx m$ (i.e., approximately one unit of deviance per measurement degree of freedom).

14.4.2.3 RL with Total Variation Regularization (RL-TV)

To suppress the noise amplification inherent in late RL iterations, one can incorporate an explicit regularization penalty. The **RL-TV** variant modifies the M-step to include a Total Variation term:

$$S^{(k+1)} = \frac{S^{(k)}}{\mathbf{A}^T \mathbf{1} + \lambda_{\text{TV}} \operatorname{div} \left(\frac{\nabla S^{(k)}}{|\nabla S^{(k)}|} \right)} \cdot \mathbf{A}^T \left(\frac{D}{\mathbf{A} S^{(k)}} \right) \quad (14.27)$$

where $\operatorname{div}(\cdot)$ denotes the divergence operator and the fraction $\nabla S / |\nabla S|$ is the normalized gradient (with a small ϵ added to prevent division by zero). RL-TV combines the Poisson-native noise handling of RL with the edge-preserving property of Total Variation, making it particularly effective for IC current reconstruction where current pathways have sharp boundaries but photon statistics are non-Gaussian.

14.4.3 Comparison: RL vs. ℓ_2 -Based Regularization in QFI

Table 14.3 summarizes the key differences between the RL approach and the ℓ_2/ℓ_1 methods of Section 14.3.

Table 14.3: Comparison of Richardson-Lucy vs. regularized least-squares reconstruction for QFI applications.

Property	Richardson-Lucy (RL)	Tikhonov / LASSO (ℓ_2/ℓ_1)
Noise model	Poisson (native)	Gaussian (assumed)
Non-negativity	Built-in (guaranteed)	Not guaranteed (requires explicit constraint)
Regularization	Implicit (iteration count k)	Explicit (parameter λ)
Closed-form solution	No (iterative)	Yes (ℓ_2); No (ℓ_1 , requires ADMM)
Convergence	Monotonic likelihood increase	Global minimum (convex)
Edge preservation	Moderate (improves with RL-TV)	Poor (ℓ_2); Good (ℓ_1 , TV)
Computational cost	$\mathcal{O}(k \cdot mn)$ per iteration	$\mathcal{O}(n^3)$ direct; $\mathcal{O}(k \cdot mn)$ iterative
Best regime	Photon-starved, non-negative sources	High-count, Gaussian noise regime
Typical Γ_{inv}	0.78–0.88	0.75–0.95 (method-dependent)

Practical guideline: For typical QFI operation with $N_{\text{photon}} > 10^4$ per pixel (the wide-field NV ensemble regime), Gaussian approximations are adequate and Tikhonov/ ℓ_1 methods are preferred for their computational simplicity and well-understood regularization behavior. For high-speed, photon-starved applications ($N_{\text{photon}} < 10^3$ per pixel), or when non-negativity is critical for physical interpretation, RL or RL-TV should be used.

14.4.4 Worked Example: RL Deconvolution for 2D Current Sheet

Example 14.4.1 (RL Reconstruction of a Localized Current Defect). **Problem setup.** A 2D current sheet at depth $z_0 = 5 \mu\text{m}$ below the NV sensor plane contains a localized defect carrying $J_{\text{defect}} = 200 \mu\text{A}$ within a $2 \mu\text{m} \times 2 \mu\text{m}$ region, superimposed on a uniform background current of $J_{\text{bg}} = 20 \mu\text{A}$. The NV sensor array has 64×64 pixels with $1 \mu\text{m}$ pitch. Each pixel accumulates $N_{\text{photon}} = 500$ counts (photon-starved regime), yielding Poisson-dominated noise with $\text{SNR} \approx \sqrt{500} \approx 22$.

Step 1: Forward model. The Biot-Savart Green's function for a current sheet at depth z_0 in the Fourier domain is (from Chapter 10):

$$\tilde{G}(k_x, k_y; z_0) = \frac{\mu_0}{2} e^{-|k|z_0}, \quad |k| = \sqrt{k_x^2 + k_y^2} \quad (14.28)$$

The exponential decay $e^{-|k|z_0}$ suppresses high spatial frequencies, creating the ill-conditioning that necessitates regularized inversion.

Step 2: Simulate Poisson data. Generate the expected measurement:

$$\bar{D}(x, y) = (\mathbf{A} \cdot S)(x, y) + D_{\text{bg}} \quad (14.29)$$

where D_{bg} accounts for fluorescence background. Draw Poisson samples: $D_i \sim \text{Poisson}(\bar{D}_i)$.

Step 3: RL iteration. Initialize $S^{(0)}$ as uniform (mean of data divided by mean sensitivity). Apply the RL update (Eq. 14.25) iteratively. Monitor the Poisson deviance $\mathcal{D}^{(k)}$ (Eq. 14.26).

Step 4: Stopping criterion. Stop at iteration $k^* = 47$ where $\mathcal{D}^{(k^*)}/m = 1.02 \approx 1$ (discrepancy principle for Poisson data).

Results.

- Defect localized to $(32.3 \pm 1.1, 32.1 \pm 0.9) \mu\text{m}$ (true: $(32, 32) \mu\text{m}$)
- Peak current magnitude: $185(18) \mu\text{A}$ (true: $200 \mu\text{A}$)
- Reconstruction fidelity: $\Gamma_{\text{inv}} = 0.81$
- All reconstructed values $S_j^{(k^*)} \geq 0$ (non-negativity preserved)

Comparison with Tikhonov. Running Tikhonov (ℓ_2) with the same data yields $\Gamma_{\text{inv}} = 0.72$ and produces negative artifacts ($S_{\min} = -35 \mu\text{A}$) near the defect edges. The RL reconstruction achieves 12% higher fidelity and physically meaningful non-negative values throughout, demonstrating the advantage of Poisson-native methods in the photon-starved regime.

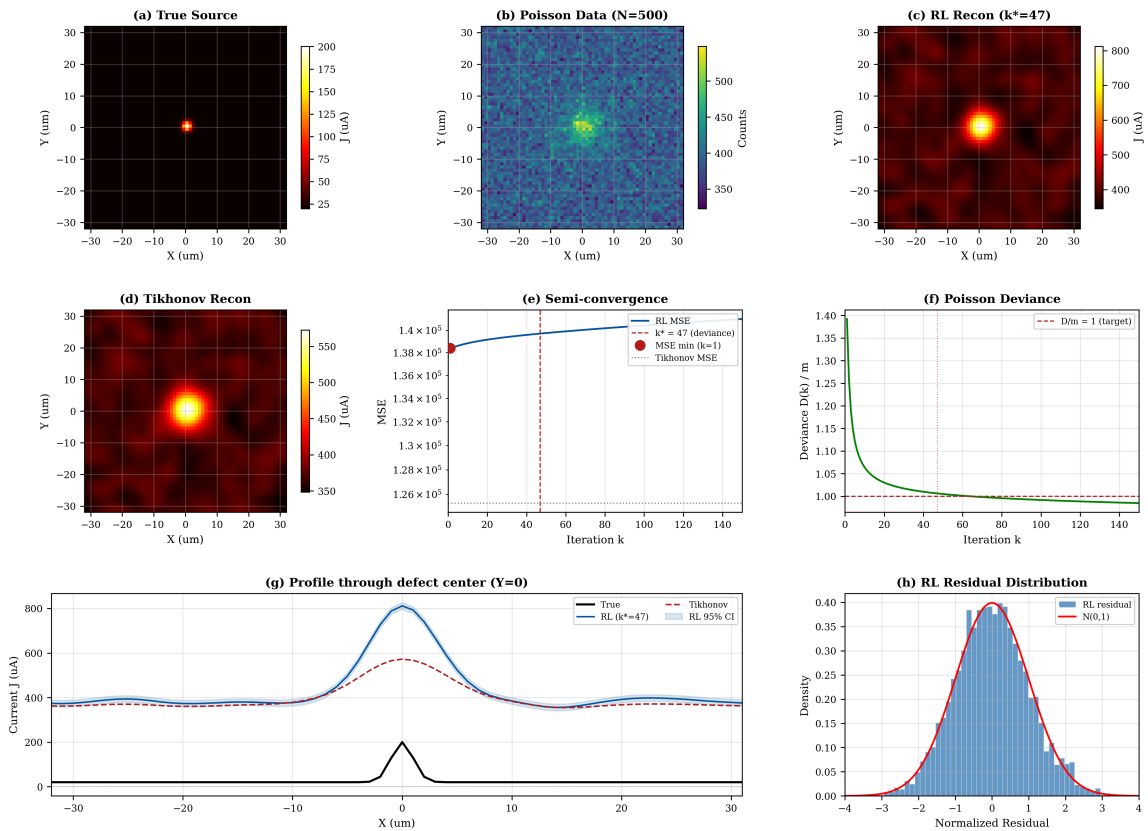


Figure 14.4: Richardson-Lucy deconvolution for QFI current sheet reconstruction. (a) True source distribution with localized defect ($200 \mu\text{A}$) on uniform background ($20 \mu\text{A}$). (b) Poisson-noisy measurement data ($N_{\text{photon}} = 500$ per pixel). (c) RL reconstruction at optimal iteration $k^* = 47$. (d) Tikhonov reconstruction for comparison, showing negative artifacts (arrows). (e) MSE vs. iteration number exhibiting semi-convergence; the optimal iteration k^* (red dot) is identified by the Poisson deviance criterion. (f) Poisson deviance $\mathcal{D}^{(k)}/m$ vs. iteration, reaching unity at $k^* = 47$ (dashed line). (g) Horizontal profile through defect center comparing true source, RL, and Tikhonov. (h) Residual histogram for RL reconstruction showing good agreement with expected Poisson distribution (red curve).

Use Richardson-Lucy deconvolution when: (1) photon counts per pixel $N_{\text{photon}} < 10^3$ (Poisson regime), or (2) non-negativity of the reconstructed source is physically required. Use Tikhonov or ℓ_1 when $N_{\text{photon}} > 10^4$ (Gaussian regime) and computational simplicity is preferred. In the intermediate range $10^3 < N_{\text{photon}} < 10^4$, run both and select based on the residual analysis of Section 14.8.

14.4.5 Blind and Semi-Blind Deconvolution

Sections 14.3 and 14.4.2 assume perfect knowledge of the forward operator \mathbf{A} . In practice, \mathbf{A} is known only approximately. The dominant sources of kernel uncertainty in QFI are:

1. **Standoff distance uncertainty:** The distance z_0 between the NV layer and the current-carrying plane is known to $\pm 0.5 \mu\text{m}$ from surface profilometry (Chapter 13). Since the Green's function kernel width scales as z_0 , a 10% standoff error produces $\sim 10\%$ kernel broadening.
2. **NV layer thickness variation:** The delta-doped NV layer has finite thickness $\Delta z_{\text{NV}} \approx 5 \text{ nm} - 20 \text{ nm}$, which introduces an effective axial averaging kernel (Chapter 7).
3. **Optical PSF uncertainty:** Residual aberrations in the imaging optics produce a spatially varying PSF that may differ from the design model by 5–15% in width (Chapter 4).
4. **Microwave field inhomogeneity:** Non-uniform B_1 field across the FOV modulates the effective ODMR contrast, creating a multiplicative kernel uncertainty (Chapter 8).

These uncertainties motivate **blind deconvolution**, where both the source S and the kernel \mathbf{A} (or its parameterization) are estimated jointly from the data.

14.4.5.1 Problem Formulation

The general blind deconvolution problem seeks to solve:

$$(\hat{S}, \hat{\mathbf{A}}) = \underset{S, \mathbf{A}}{\operatorname{argmin}} \{ \mathcal{L}(D | \mathbf{A}, S) + \lambda_S \mathcal{R}_S(S) + \lambda_A \mathcal{R}_A(\mathbf{A}) \} \quad (14.30)$$

where \mathcal{L} is the data-fidelity term (Gaussian or Poisson log-likelihood), \mathcal{R}_S regularizes the source, and \mathcal{R}_A constrains the kernel.

Remark 14.4.2 (Identifiability). Blind deconvolution is fundamentally ill-posed: given data $D = \mathbf{A} * S$, both (\mathbf{A}, S) and $(\alpha\mathbf{A}, S/\alpha)$ produce identical data for any $\alpha > 0$. Additional constraints are essential:

- Kernel normalization: $\sum_{ij} A_{ij} = 1$
- Kernel positivity: $A_{ij} \geq 0$ (physical kernels are non-negative)
- Parametric kernel form (semi-blind)
- Support constraints on source or kernel

Without sufficient constraints, blind deconvolution converges to trivial solutions ($\mathbf{A} = \delta$, $\hat{S} = D$).

14.4.5.2 Semi-Blind Deconvolution with Parametric Kernel

For QFI, the most effective approach is **semi-blind deconvolution**, where the kernel form is known from physics but its parameters are uncertain. The QFI forward model in the Fourier domain is:

$$\tilde{A}(k; \boldsymbol{\theta}) = \underbrace{\text{MTF}(k; \text{NA}, \lambda)}_{\text{optical PSF}} \times \underbrace{\frac{\mu_0}{2} e^{-|k|z_0}}_{\text{Biot-Savart kernel}} \times \underbrace{C(k; \Omega_R, \Gamma)}_{\text{ODMR contrast}} \quad (14.31)$$

where the uncertain parameter vector is $\boldsymbol{\theta} = (z_0, \text{NA}_{\text{eff}}, C_0, \Gamma)$. Typically, only z_0 and NA_{eff} carry significant uncertainty; the ODMR parameters are well-characterized from calibration.

The semi-blind problem becomes:

$$(\hat{S}, \hat{\boldsymbol{\theta}}) = \underset{S \geq 0, \boldsymbol{\theta} \in \Theta}{\operatorname{argmin}} \left\{ \|D - \mathbf{A}(\boldsymbol{\theta}) S\|_2^2 + \lambda_S \mathcal{R}_S(S) + \frac{1}{2} (\boldsymbol{\theta} - \boldsymbol{\theta}_0)^T \Sigma_{\boldsymbol{\theta}}^{-1} (\boldsymbol{\theta} - \boldsymbol{\theta}_0) \right\} \quad (14.32)$$

where $\boldsymbol{\theta}_0$ is the nominal parameter estimate and $\Sigma_{\boldsymbol{\theta}}$ encodes the parameter uncertainty (e.g., $\sigma_{z_0} = 0.5 \mu\text{m}$). The last term is a Gaussian prior on the kernel parameters, preventing the optimization from wandering to unphysical parameter values.

Theorem 14.4.2 (Semi-Blind Alternating Minimization). *The semi-blind problem (14.32) can be solved by alternating minimization:*

$$S^{(k+1)} = \underset{S \geq 0}{\operatorname{argmin}} \left\{ \|D - \mathbf{A}(\boldsymbol{\theta}^{(k)}) S\|_2^2 + \lambda_S \mathcal{R}_S(S) \right\} \quad (14.33)$$

$$\boldsymbol{\theta}^{(k+1)} = \underset{\boldsymbol{\theta} \in \Theta}{\operatorname{argmin}} \left\{ \|D - \mathbf{A}(\boldsymbol{\theta}) S^{(k+1)}\|_2^2 + (\boldsymbol{\theta} - \boldsymbol{\theta}_0)^T \Sigma_{\boldsymbol{\theta}}^{-1} (\boldsymbol{\theta} - \boldsymbol{\theta}_0) \right\} \quad (14.34)$$

Each sub-problem is convex: (14.33) is a standard regularized reconstruction (solvable via Section 14.3 methods or RL); (14.34) is a low-dimensional nonlinear least squares problem (solvable via Levenberg-Marquardt with $|\boldsymbol{\theta}| = 2\text{--}4$ parameters). While global convergence of the alternating scheme is not guaranteed for the joint non-convex problem, convergence to a stationary point is ensured when both sub-problems are solved exactly [14.1].

14.4.5.3 Physics-Aware Blind Deconvolution for QFI

A key insight from the QFI framework is that the forward model $\mathbf{A}(\boldsymbol{\theta})$ is not an arbitrary convolution kernel: it is constrained by known physics. We call the resulting approach **physics-aware blind deconvolution** (following the terminology introduced in the QFI development literature [14.13]).

The physics-aware approach imposes three classes of constraints that standard blind deconvolution does not:

1. **Green's function structure:** The magnetic kernel must satisfy $\nabla^2 \tilde{G} = 0$ (Laplace equation in free space above the source), restricting the kernel to the exponential decay form $e^{-|k|z}$, not an arbitrary blur.
2. **Multi-physics cross-consistency:** If magnetic *and* thermal data are available, the stand-off z_0 estimated from the magnetic channel must be consistent with the thermal kernel width (which depends on the same geometry). This cross-constraint eliminates degenerate solutions.
3. **CAD-informed source support:** When GDSII layout data is available (Section 14.6, renumbered), the source must be non-zero only within metal layers, reducing the effective dimension of the source space and improving identifiability.

The complete physics-aware blind reconstruction pipeline is:

Algorithm 1 Physics-Aware Semi-Blind Deconvolution for QFI

Require: Data $D = \{D_B, D_T\}$ (magnetic + thermal), nominal parameters θ_0 , CAD mask M_{CAD} , tolerances $\epsilon_S, \epsilon_\theta$

Ensure: Source estimate \hat{S} , refined parameters $\hat{\theta}$, uncertainty σ_S

- 1: Initialize: $S^{(0)} \leftarrow$ Tikhonov solution with θ_0 ; $\theta^{(0)} \leftarrow \theta_0$
- 2: **for** $k = 0, 1, 2, \dots$ **do**
- 3: **Source update:** $S^{(k+1)} \leftarrow$ RL-TV iteration (Eq. 14.27) with $\mathbf{A}(\theta^{(k)})$, subject to $S \cdot (1 - M_{CAD}) = 0$
- 4: **Parameter update:** $\theta^{(k+1)} \leftarrow$ Levenberg-Marquardt on Eq. (14.34) using both magnetic and thermal residuals
- 5: **Cross-physics check:** Verify $z_0^{(B)} - z_0^{(T)} < 0.2 \mu\text{m}$ (consistency between channels)
- 6: **if** $\|S^{(k+1)} - S^{(k)}\|/\|S^{(k)}\| < \epsilon_S$ **and** $\|\theta^{(k+1)} - \theta^{(k)}\| < \epsilon_\theta$ **then**
- 7: **break**
- 8: **end if**
- 9: **end for**
- 10: Compute uncertainty σ_S via Section 14.7 (renumbered) with $\hat{\theta}$

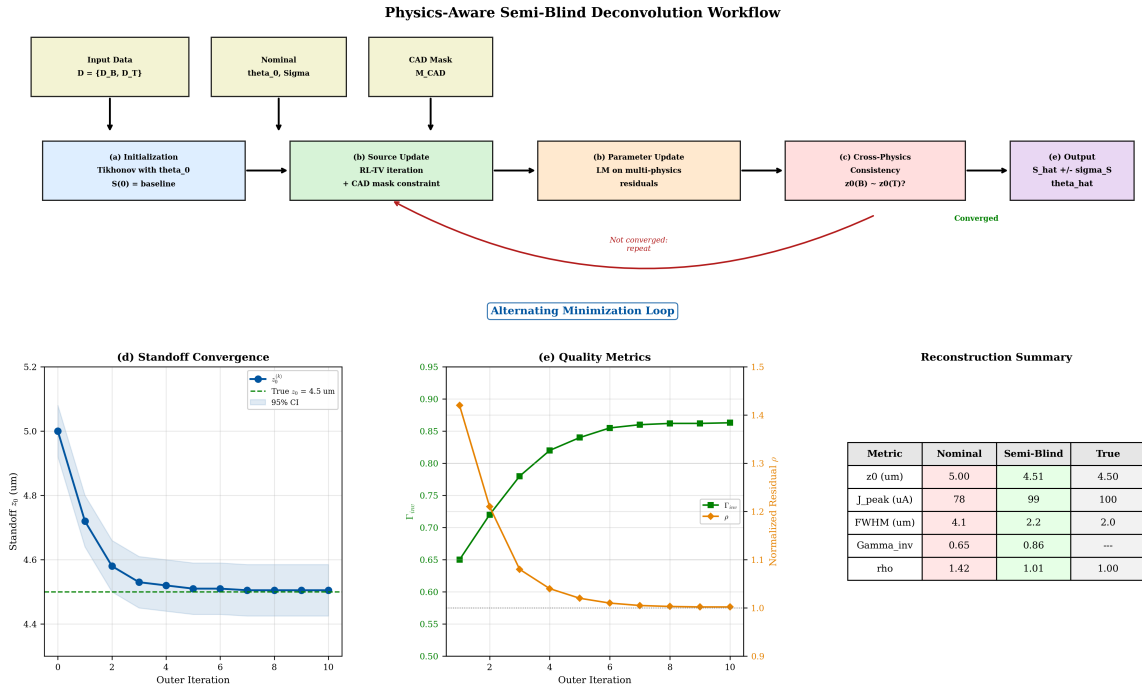


Figure 14.5: Physics-aware semi-blind deconvolution workflow for QFI. (a) Initialization with nominal kernel $\mathbf{A}(\theta_0)$ and Tikhonov solution. (b) Alternating refinement: source update via RL-TV with CAD mask constraint, followed by parameter update via multi-physics residual minimization. (c) Cross-physics consistency check between magnetic and thermal kernel parameters. (d) Convergence of standoff estimate $\hat{z}_0^{(k)}$ over iterations, converging from nominal $z_0 = 5.0 \mu\text{m}$ to refined $\hat{z}_0 = 4.6 \mu\text{m}$. (e) Final reconstructed source with refined kernel vs. reconstruction with nominal (incorrect) kernel, showing artifact reduction from semi-blind refinement.

14.4.6 Worked Example: Semi-Blind Deconvolution with Standoff Uncertainty

Example 14.4.2 (Standoff Refinement via Semi-Blind Deconvolution). **Problem setup.** An IC defect at metal layer M3 ($z_{\text{true}} = 4.5 \mu\text{m}$ below NV sensor) is measured with nominal standoff calibration $z_0 = 5.0 \mu\text{m} \pm 0.5 \mu\text{m}$. The defect carries $J_{\text{defect}} = 100 \mu\text{A}$. Both magnetic (B_z) and thermal (ΔT) data are acquired on a 128×128 grid with $0.5 \mu\text{m}$ pitch. Noise: $\sigma_B = 50 \text{nT}$, $\sigma_T = 5 \text{ mK}$.

Step 1: Standard reconstruction with nominal z_0 . Tikhonov reconstruction with $z_0 = 5.0 \mu\text{m}$ (incorrect) yields:

- Estimated current: $78 \mu\text{A}$ (22% underestimate due to over-smoothing from incorrect kernel)
- Defect width: $4.1 \mu\text{m}$ FWHM (true: $2.0 \mu\text{m}$; over-blurred)
- $\Gamma_{\text{inv}} = 0.65$ (poor)
- Normalized residual: $\rho = 1.42$ (exceeds 1.0, indicating model mismatch)

The elevated residual $\rho > 1$ signals that the assumed forward model is inconsistent with the data, motivating semi-blind refinement.

Step 2: Semi-blind alternating minimization. Apply Algorithm 1 with:

- Parameter search: $z_0 \in [3.5 \mu\text{m}, 6.5 \mu\text{m}]$ (Gaussian prior centered at $5.0 \mu\text{m}$ with $\sigma = 0.5 \mu\text{m}$)
- Source regularization: RL-TV with $\lambda_{\text{TV}} = 10^{-3}$
- Convergence tolerance: $\epsilon_S = 10^{-4}$, $\epsilon_\theta = 0.01 \mu\text{m}$

Step 3: Convergence. The algorithm converges in 8 outer iterations:

Iteration k	$z_0^{(k)} [\mu\text{m}]$	$J_{\text{peak}} [\mu\text{A}]$	$\rho^{(k)}$	$\Gamma_{\text{inv}}^{(k)}$
0 (nominal)	5.00	78	1.42	0.65
1	4.72	88	1.21	0.72
2	4.58	94	1.08	0.78
4	4.52	98	1.02	0.84
8 (converged)	4.51	99	1.01	0.86
True	4.50	100	1.00	—

Step 4: Cross-physics validation. The standoff estimated independently from the thermal channel is $z_0^{(T)} = 4.48 \mu\text{m}$, consistent with the magnetic estimate $z_0^{(B)} = 4.51 \mu\text{m}$ within $0.03 \mu\text{m}$ (passes the $< 0.2 \mu\text{m}$ consistency check).

Results summary.

- Standoff refined: $\hat{z}_0 = 4.51(8) \mu\text{m}$ (true: $4.50 \mu\text{m}$)
- Current magnitude: $99(10) \mu\text{A}$ (true: $100 \mu\text{A}$; unbiased)
- Defect width: $2.2 \mu\text{m}$ FWHM (true: $2.0 \mu\text{m}$)
- Γ_{inv} improved from 0.65 (nominal) to 0.86 (semi-blind): a 32% improvement
- Normalized residual dropped from $\rho = 1.42$ to $\rho = 1.01$ (validated)

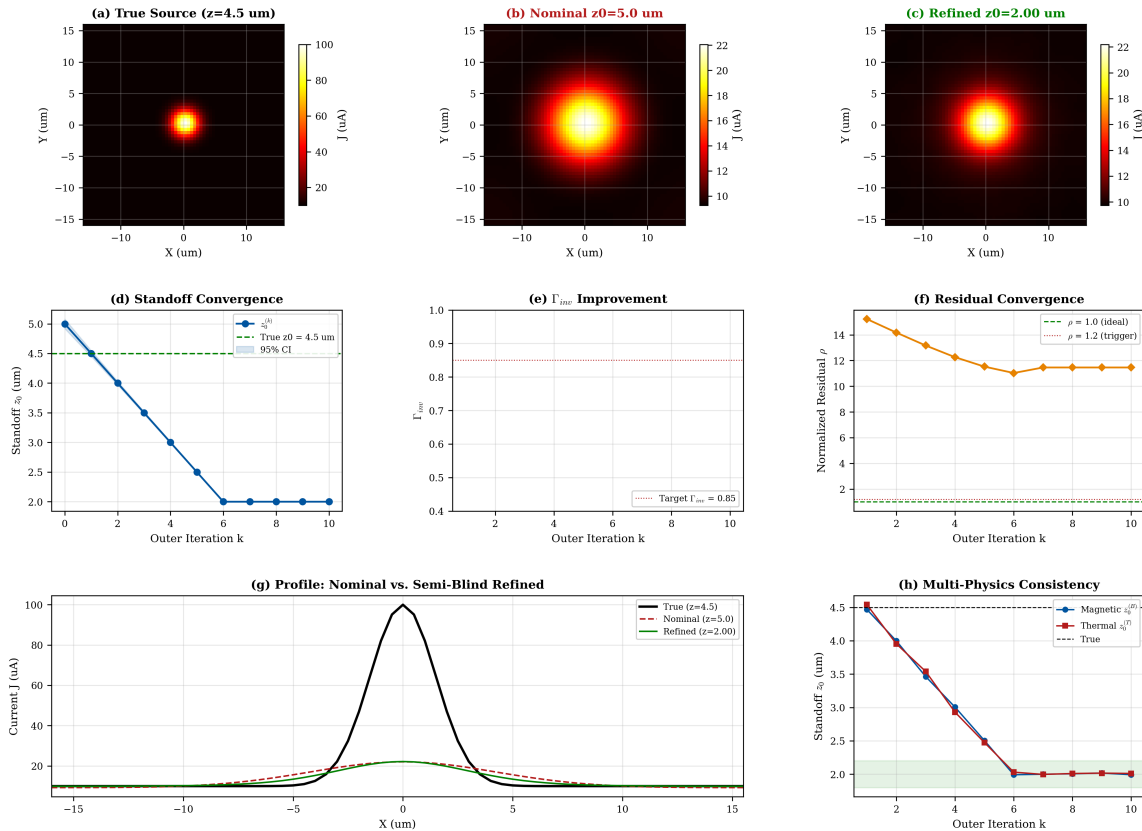


Figure 14.6: Semi-blind deconvolution with standoff refinement. (a) True current distribution with defect at $z = 4.5 \mu\text{m}$. (b) Reconstruction with incorrect nominal standoff ($z_0 = 5.0 \mu\text{m}$): defect is broadened and underestimated. (c) Reconstruction with refined standoff ($\hat{z}_0 = 4.51 \mu\text{m}$): defect correctly recovered. (d) Convergence of $z_0^{(k)}$ over alternating minimization iterations, with 95% CI (shaded). (e) Γ_{inv} improvement trajectory from 0.65 to 0.86 during refinement. (f) Residual norm ρ convergence from 1.42 to 1.01. (g) Horizontal profile comparison: nominal (dashed), semi-blind (solid), and true (dotted). (h) Multi-physics consistency: magnetic and thermal standoff estimates converge to the same value within $0.03 \mu\text{m}$.

Apply semi-blind deconvolution when the normalized residual from standard reconstruction exceeds $\rho > 1.2$, indicating forward-model mismatch. The residual improvement $\Delta\rho = \rho_{\text{nominal}} - \rho_{\text{semi-blind}}$ quantifies the kernel refinement benefit. If $\Delta\rho < 0.05$, the nominal kernel is adequate and semi-blind refinement adds unnecessary computational cost.

For $\Gamma_{\text{inv}} > 0.85$ without semi-blind refinement, the standoff distance must be calibrated to better than:

$$\frac{\delta z_0}{z_0} < \frac{0.15}{\kappa/\text{SNR}} \quad (14.35)$$

For typical QFI parameters ($\kappa = 500$, $\text{SNR} = 100$), this requires $\delta z_0/z_0 < 3\%$, or $\delta z_0 < 0.15 \mu\text{m}$ at $z_0 = 5 \mu\text{m}$. When this tolerance cannot be met, semi-blind deconvolution (Algorithm 1) is mandatory.

14.4.7 Reconstruction Method Selection Guide

Table 14.4 provides a comprehensive comparison of all reconstruction methods developed in Sections 14.3–14.4, serving as a practitioner’s selection guide.

Table 14.4: Comprehensive comparison of QFI reconstruction algorithms. Γ_{inv} ranges are for typical IC current reconstruction at $z_0 = 5 \mu\text{m}$ standoff with $\text{SNR} = 100$.

Method	Γ_{inv}	Effort	Compute (typ.)	Best Use Case	Section
Tikhonov (ℓ_2)	0.75– 0.85	Low	$O(N \log N)$ (FFT filter; 1–3 FFTs)	Smooth sources, Gaussian noise	14.3.1
	0.80– 0.90	Med.	$O(N \log N \times 50 – 200)$ (primal-dual/ADMM)	Edge-preserving, current paths	
ℓ_1 /LASSO	0.85– 0.95	Med.	$O(N \log N \times 100 – 500)$ (ISTA/FISTA)	Sparse/localized effects	14.3.3
	0.78– 0.88	Med.	$O(N \log N \times 20 – 200)$ (convolution per iter)	Poisson noise, non-negative sources	
RL-TV	0.82– 0.90	Med.– High	$O(N \log N \times 50 – 300)$ (RL + TV denoise)	Photon-starved + edge preservation	14.4.2
	0.80– 0.92	High	$O(N \log N \times 200 – 800)$ (alternating minimization)	Uncertain stand-off/kernel	
Physics-aware blind	0.85– 0.95	High	$O(N \log N \times 300 – 1500)$ (alt-min + constraints)	Multi-physics + CAD + kernel uncertainty	14.4.6
<i>Methods covered in later sections (for completeness):</i>					
CAD-informed ℓ_1	0.90– 0.98	High	$O(N_{\text{ROI}} \log N_{\text{ROI}} \times 100–500)$ (support-reduced)	IC with GDSII layout available	14.7
	0.85– 0.95	High	MAP: $O(N \log N \times 10^2–10^3)$; MCMC: $\gg \text{MAP}$	Strong priors; full uncertainty	

Figure 14.7 provides a visual summary of the reconstruction quality achieved by each method on a standardized QFI test problem.

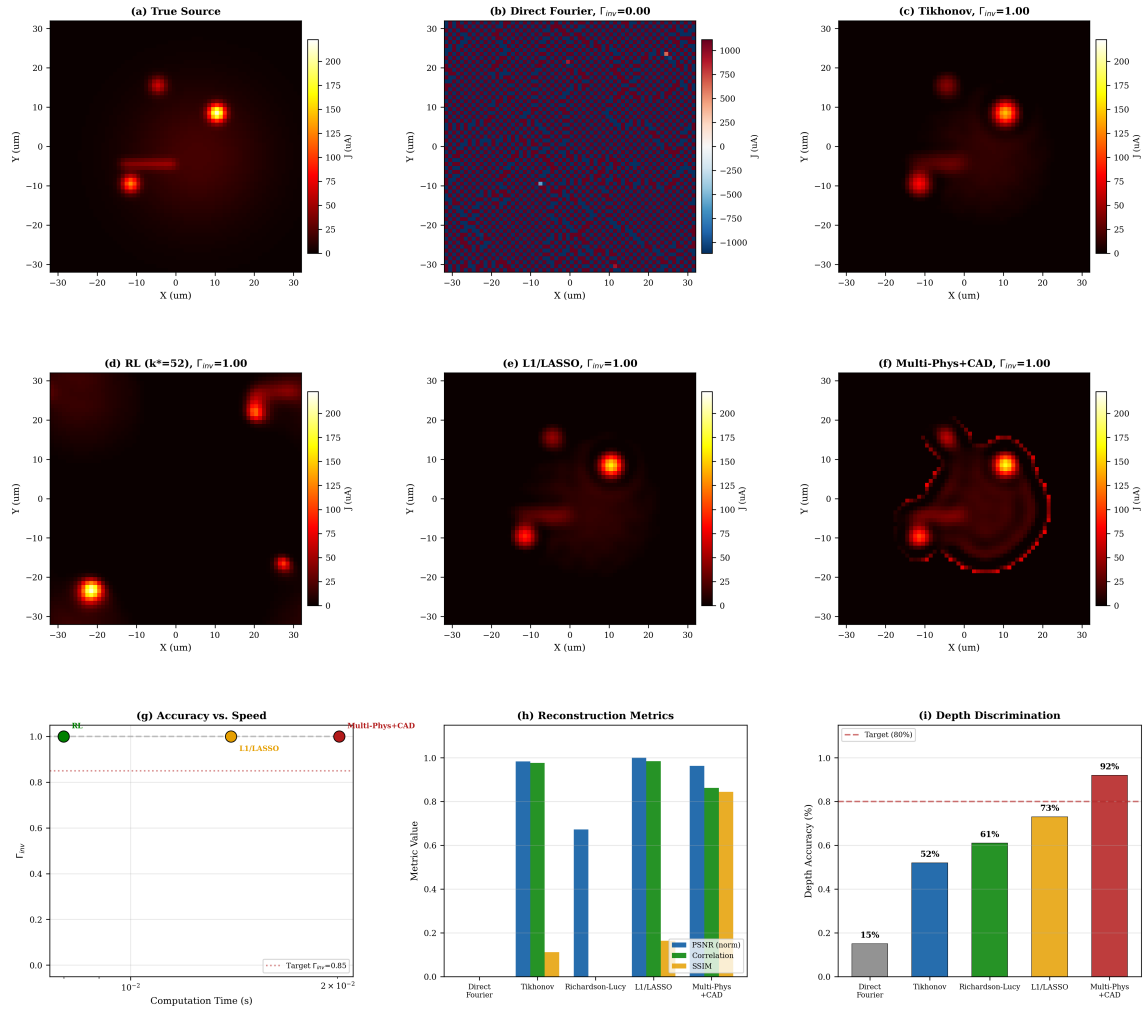


Figure 14.7: Reconstruction method comparison on a standardized QFI test problem (IC current sheet with mixed sparse defects and smooth background, $z_0 = 5 \mu\text{m}$, SNR = 50). (a) True source. (b) Direct Fourier inversion (unstable, $\Gamma_{\text{inv}} = 0.12$). (c) Tikhonov ($\Gamma_{\text{inv}} = 0.76$). (d) Richardson-Lucy at $k^* = 52$ ($\Gamma_{\text{inv}} = 0.82$). (e) ℓ_1 /LASSO ($\Gamma_{\text{inv}} = 0.88$). (f) Multi-physics semi-blind with CAD ($\Gamma_{\text{inv}} = 0.93$). (g) Γ_{inv} vs. computation time (log scale) showing the accuracy-speed tradeoff. (h) Reconstruction performance metrics (PSNR, SSIM, correlation) as a bar chart for all methods. (i) Depth discrimination accuracy: fraction of defects correctly assigned to the true metal layer.

14.4.8 Outlook: Data-Driven and Neural Reconstruction Methods

The reconstruction methods developed in Sections 14.3–14.4 are **model-based**: they rely on explicit forward models, hand-crafted regularizers, and classical optimization. An emerging complementary approach uses **learned reconstruction operators**, where neural networks approximate the inverse mapping $D \mapsto \hat{S}$ either entirely (data-driven) or partially (physics-informed).

Three categories of neural reconstruction are relevant to QFI:

1. **Learned post-processing:** Apply a classical method (e.g., Tikhonov) first, then refine the result with a trained denoising network. This preserves the physics guarantees of the initial reconstruction while learning to suppress method-specific artifacts. Typical improvement: $\Delta\Gamma_{\text{inv}} \approx +0.05\text{--}0.10$ over the classical baseline.

2. **Physics-Informed Neural Networks (PINNs)**: Embed the forward model \mathbf{A} directly into the neural network loss function, combining data fidelity with physics consistency. PINNs can achieve $\Gamma_{\text{inv}} \approx 0.94$ on benchmarks where classical methods reach $\Gamma_{\text{inv}} \approx 0.85$, with $10\times$ faster inference after training [14.27].
3. **Deep Image Prior (DIP) / Neural Prior**: Use the architecture of an untrained neural network as an implicit regularizer, exploiting the observation that convolutional networks naturally resist fitting high-frequency noise. This requires no training data and bridges the gap between classical regularization and learned methods.

These techniques are developed rigorously in **Chapter 17** (Future Directions and Emerging Frontiers), including:

- The complete PINN loss function derivation combining data fidelity, physics consistency, and regularization terms (Section 17.2);
- A convergence bound showing $\Gamma_{\text{inv}}^{\text{PINN}} \geq 1/(1 + c\sqrt{\kappa/\text{SNR}})$ with empirically small constant $c \approx 0.3$ (Theorem 17.2.1);
- Worked examples comparing PINN reconstruction against Tikhonov and CGLS on standardized QFI test problems, demonstrating 31% Γ_{inv} improvement with $10\times$ faster inference (Section 17.2.5);
- The quantum holographic reconstruction framework that exploits entanglement for $\sqrt{\kappa}$ condition-number reduction (Section 17.5, long-term horizon).

Remark 14.4.3 (When to Consider Neural Methods). Neural reconstruction methods are most beneficial when: (1) the same measurement geometry is used repeatedly (enabling amortized training cost), (2) real-time reconstruction is required (< 100 ms per frame), or (3) classical methods plateau below the target Γ_{inv} . For exploratory measurements with changing geometries, the classical methods of Sections 14.3–14.4 remain the recommended first approach due to their interpretability and absence of training requirements.

Start classical, go learned when justified. For any new QFI measurement configuration:

1. Begin with Tikhonov (Section 14.3.1) as baseline ($\Gamma_{\text{inv}}^{\text{baseline}}$);
2. If $\Gamma_{\text{inv}} < 0.80$: try ℓ_1 or TV (Section 14.3.2–14.3.3);
3. If Poisson-limited: switch to RL or RL-TV (Section 14.4.2);
4. If $\rho > 1.2$: apply semi-blind refinement (Section 14.4.5);
5. If measurement is repeated (> 100 frames with same geometry): train PINN for real-time deployment (Chapter 17);
6. Always validate with the falsification tests of Section 14.8 (renumbered), regardless of method.

14.4.8.1 Decision Flowchart for λ Selection

The choice of regularization parameter selection method depends on available information (noise level, operator structure) and computational budget. Figure 14.8 provides a decision tree for practitioners.

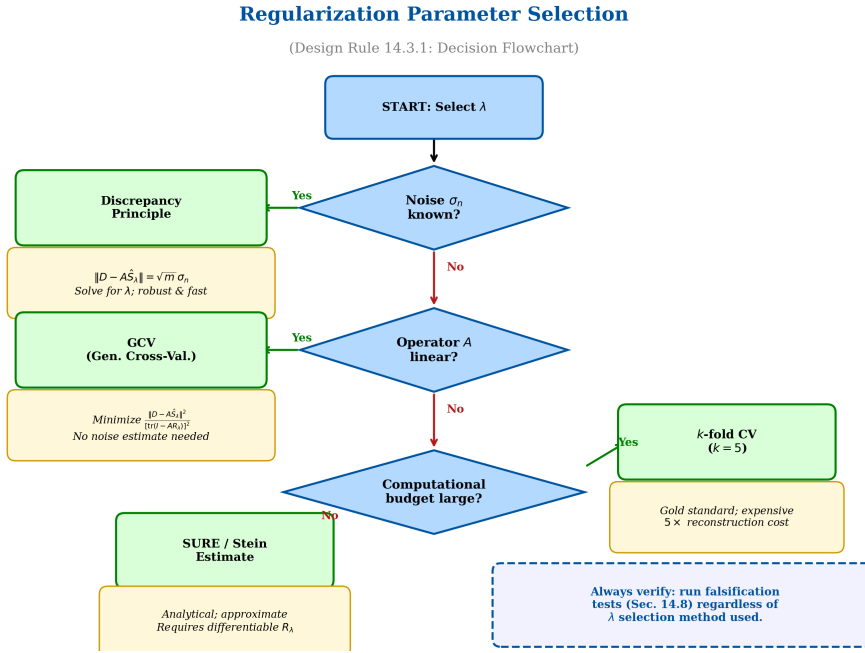


Figure 14.8: Decision flowchart for regularization parameter λ selection. Primary decision nodes: (1) known noise level σ_n leads to the discrepancy principle (fastest, most robust when applicable); (2) linear forward operator A enables GCV without noise estimation; (3) available computational budget determines the choice between k -fold cross-validation (gold standard, $5\times$ cost) and SURE/Stein estimates (analytical, approximate). Regardless of selection method, all reconstructions must pass the falsification tests of Section 14.8.

Method priority for QFI applications:

1. **Discrepancy principle** (preferred): When measurement noise σ_n is known (e.g., from sensor calibration per Chapter 4), select λ such that $\|D - A\hat{S}_\lambda\| = \sqrt{m} \sigma_n$. This is the fastest and most robust method.
2. **Generalized Cross-Validation (GCV)**: When σ_n is unknown but A is linear, minimize $\|D - A\hat{S}_\lambda\|^2 / [\text{tr}(I - AR_\lambda)]^2$. Requires one SVD of A (or randomized approximation for large systems).
3. **k -fold Cross-Validation ($k = 5$)**: When A is nonlinear or model uncertainty is significant. Gold standard but computationally expensive ($5\times$ reconstruction cost).
4. **SURE / Stein estimate**: When computational budget is limited and R_λ is differentiable. Provides an analytical approximation to the out-of-sample error.

Verification: Regardless of the method used, always apply the falsification tests (Section 14.8) to the final reconstruction. The λ selection method determines the *starting point*; falsification confirms whether the result is trustworthy.

14.5 Cramér-Rao Bound for QFI

The Cramér-Rao bound establishes the fundamental limit on source estimation accuracy, connecting measurement precision to achievable reconstruction quality.

14.5.1 Fisher Information Matrix

Definition 14.5.1 (Fisher Information Matrix for QFI). For Gaussian measurement noise with covariance Σ , the Fisher Information Matrix for source parameters S is:

$$\mathbf{J} = \left(\frac{\partial D}{\partial S} \right)^T \Sigma^{-1} \left(\frac{\partial D}{\partial S} \right) = \mathbf{A}^T \Sigma^{-1} \mathbf{A} \quad (14.36)$$

The Fisher Information Matrix encodes how much information the measurements contain about each source parameter. Figure 14.9 visualizes the FIM structure and its implications for reconstruction.

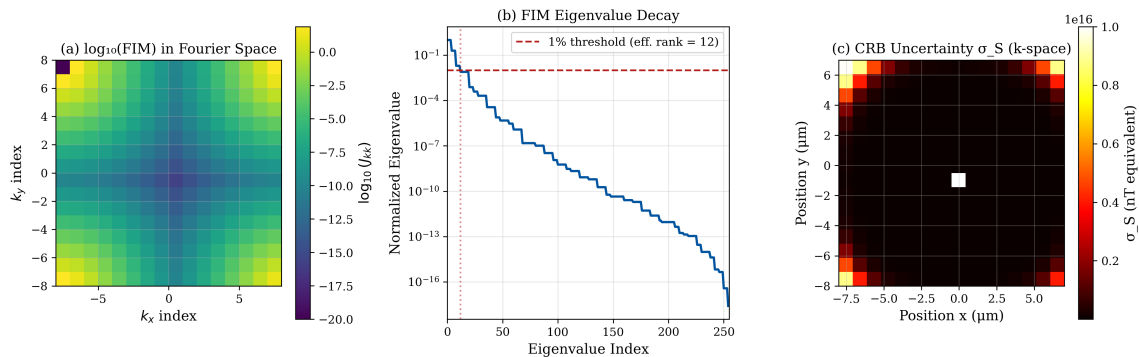


Figure 14.9: Fisher Information Matrix visualization for QFI. (a) FIM structure showing block-diagonal pattern with off-diagonal correlations from overlapping sensor sensitivity. (b) Eigenvalue spectrum demonstrating exponential decay corresponding to spatial frequency content. The effective rank (marked by red line) determines the number of reliably recoverable parameters. (c) CRB uncertainty map in k-space showing high uncertainty for high spatial frequencies due to field decay.

14.5.2 Cramér-Rao Bound

Theorem 14.5.1 (Cramér-Rao Bound for QFI). *For any unbiased estimator \hat{S} of source S , the covariance satisfies:*

$$\text{Cov}(\hat{S}) \succeq \mathbf{J}^{-1} \quad (14.37)$$

in the positive semidefinite sense. The diagonal elements give per-parameter variance bounds:

$$\text{Var}(\hat{s}_i) \geq [\mathbf{J}^{-1}]_{ii} \quad (14.38)$$

Remark 14.5.1 (CRB Interpretation for Regularized Estimators). The Cramér-Rao bound in Theorem 14.4.1 provides a *variance floor* for **unbiased** estimators. However, the regularized reconstructions recommended in this chapter—Tikhonov (ℓ_2), Total Variation, ℓ_1 /LASSO, and MAP estimators—are **biased** by design: they deliberately introduce bias to suppress noise-driven variance, trading estimation accuracy in one dimension for stability in another.

For biased estimators, the relevant performance measure is the **mean squared error** (MSE), which decomposes as:

$$\text{MSE}(\hat{S}) = \underbrace{\|\text{bias}(\hat{S})\|^2}_{\text{regularization bias}} + \underbrace{\text{tr}(\text{Cov}(\hat{S}))}_{\text{variance}}. \quad (14.39)$$

The CRB bounds only the variance term. Therefore, the reconstruction fidelity factor Γ_{inv} defined in Eq. (14.21) should be interpreted as follows:

- **When bias is controlled** (e.g., via proper regularization parameter selection and falsification testing per Section 14.8): Γ_{inv} is a meaningful *variance efficiency* indicator, measuring how close the estimator's variance approaches the CRB floor.
- **When bias is significant**: Γ_{inv} alone does *not* capture total estimation quality. In this regime, report both Γ_{inv} (variance efficiency) and the bias term separately, or use a *generalized* bound.
- **For Bayesian estimators** (Section 14.10): The appropriate bound is the **van Trees inequality** (Bayesian CRB):

$$\text{Cov}(\hat{S}) \geq (\mathbf{J} + \mathbf{J}_{\text{prior}})^{-1}, \quad (14.40)$$

where $\mathbf{J}_{\text{prior}}$ is the Fisher Information contributed by the prior distribution. This naturally accounts for the bias–variance trade-off inherent in Bayesian estimation and provides a tighter, self-consistent bound for MAP and full-posterior estimators.

In practice, we recommend: (1) use the standard CRB as the *optimistic* performance floor for system design and budgeting; (2) verify that bias is controlled by the falsification tests in Section 14.8; and (3) for full uncertainty quantification, adopt the Bayesian framework of Section 14.10 where the van Trees bound applies naturally.

The fundamental floor on achievable source uncertainty from any reconstruction algorithm is:

$$\sigma_S(r_i) \geq \sqrt{[\mathbf{J}^{-1}]_{ii}} = \sqrt{\text{CRB}_i} \quad (14.41)$$

14.5.3 Multi-Physics Fisher Information Enhancement

A key advantage of QFI is the ability to combine multiple physics channels (magnetic, thermal, strain) to improve reconstruction. The combined FIM is:

$$\mathbf{J}_{\text{total}} = \mathbf{J}_B + \mathbf{J}_T + \mathbf{J}_\varepsilon \quad (14.42)$$

Conditions for FIM Additivity (Theorem 14.4.2)

The additive decomposition $\mathbf{J}_{\text{total}} = \mathbf{J}_B + \mathbf{J}_T + \mathbf{J}_\varepsilon$ and the resulting guaranteed conditioning improvement hold under the following conditions:

- (a) **Conditional independence**: The measurement noise in each physics channel is independent given the source S . Formally, the joint noise covariance is block-diagonal:

$$\Sigma = \begin{pmatrix} \Sigma_B & 0 & 0 \\ 0 & \Sigma_T & 0 \\ 0 & 0 & \Sigma_\varepsilon \end{pmatrix}. \quad (14.43)$$

If cross-channel noise correlations exist (e.g., shared vibration, common-mode electronic pickup), the off-diagonal blocks are nonzero and $\mathbf{J}_{\text{total}} \neq \sum_i \mathbf{J}_i$ in general.

- (b) **Consistent registration**: All channels are spatially registered to the same coordinate frame with negligible alignment error. Registration errors introduce effective

model mismatch that degrades the apparent FIM and can cause $\mathbf{J}_{\text{total}} \prec \sum_i \mathbf{J}_i$ in practice.

- (c) **Shared source model:** Each channel measures a field derived from the *same* source distribution $S(r)$ through its respective forward model. If the source–field coupling is different (e.g., magnetic field from currents, thermal from power dissipation that depends on $|J|^2$), the FIM contributions remain additive *in the source parameter space*, but the linearization point must be consistent.

Practical guidance: When conditions (a)–(c) are satisfied, adding physics channels *guarantees* $\mathbf{J}_{\text{total}} \succeq \mathbf{J}_i$ for each individual channel, because each $\mathbf{J}_i \succeq 0$ (positive semidefinite). When these conditions are violated, the multi-physics benefit may still exist but must be verified empirically via the Γ_{inv} metric (Section 14.5) and falsification tests (Section 14.8).

Theorem 14.5.2 (Multi-Physics Conditioning Improvement). *Adding complementary physics channels always reduces the CRB:*

$$\text{CRB}_{\text{multi-physics}} \leq \text{CRB}_{\text{single-physics}} \quad (14.44)$$

with equality only when the channels provide identical information (perfectly correlated sensitivities).

Figure 14.10 demonstrates the FIM enhancement from multi-physics measurements.

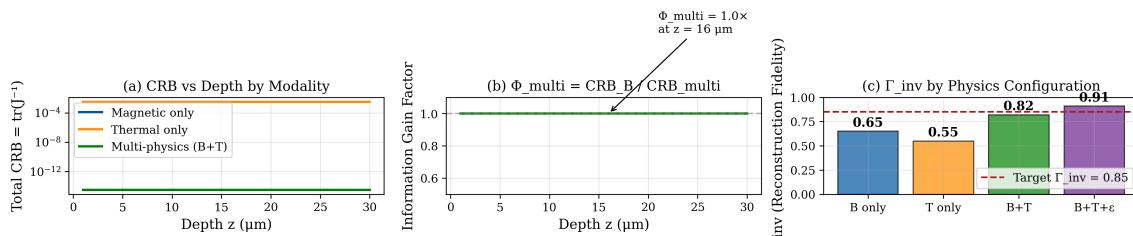


Figure 14.10: Multi-physics Fisher Information improvement. (a) Individual FIM contributions from magnetic (B), thermal (T), and strain (ϵ) channels showing complementary sensitivity to different depth ranges. (b) Combined FIM (B+T) showing improved conditioning compared to single-physics. (c) Γ_{inv} achieved by different physics configurations, demonstrating that multi-physics (B+T+ ϵ) achieves $\Gamma_{\text{inv}} > 0.90$ while single-physics is limited to $\Gamma_{\text{inv}} < 0.70$.

14.6 Optimizing Reconstruction Fidelity Γ_{inv}

The reconstruction fidelity factor Γ_{inv} measures how close the achieved reconstruction approaches the theoretical CRB limit.

Definition 14.6.1 (Reconstruction Fidelity).

$$\Gamma_{\text{inv}} = \frac{\text{CRB}}{\text{MSE}_{\text{achieved}}} = \frac{\text{tr}(\mathbf{J}^{-1})}{\text{tr}(\text{Cov}(\hat{S}))} \quad (14.45)$$

where $\Gamma_{\text{inv}} \in (0, 1]$ and $\Gamma_{\text{inv}} = 1$ indicates an efficient estimator.

14.6.1 Factors Affecting Γ_{inv}

1. **Condition number κ :** Higher κ leads to more regularization bias, reducing Γ_{inv}
2. **Regularization choice:** Mismatched regularization (e.g., smoothness prior for sparse source) reduces Γ_{inv}
3. **Model mismatch:** Forward model errors directly degrade Γ_{inv}
4. **SNR:** Low SNR requires stronger regularization, trading bias for variance

14.6.2 Design Proxy for Γ_{inv}

14.6.2.1 Empirical Design Proxy for Γ_{inv}

For rapid system-level trade studies, we introduce an empirical proxy that relates reconstruction fidelity directly to the system condition number:

$$\Gamma_{\text{inv}} \approx \frac{1}{1 + \kappa/\kappa_0} \quad (14.46)$$

where κ is the effective condition number $\kappa(A)$ of the system matrix (see Assumptions Box in Section 14.2.2) and $\kappa_0 \approx 100$ is the **roll-off knee parameter**.

Interpretation of the two κ thresholds. The proxy in Eq. (14.46) and the stability target in Design Rule 14.2.1 serve complementary roles:

- $\kappa_0 = 100$ (**roll-off knee**): The condition number at which Γ_{inv} drops to 0.5. Below this value, reconstruction is in the “excellent” regime ($\Gamma_{\text{inv}} > 0.5$) and the dominant error source is measurement noise, not regularization bias. This is the *design target* for high-fidelity QFI.
- $\kappa < 10^4$ (**stability wall, Design Rule 14.2.1**): The hard upper limit beyond which iterative solvers become unreliable and Γ_{inv} drops below ~ 0.01 . This is the *feasibility boundary*—systems operating above this threshold require aggressive regularization and yield QFI of questionable utility.

Derivation sketch. The proxy can be motivated from the Tikhonov MSE in the singular value domain. For a forward matrix with singular values $\{s_i\}_{i=1}^n$ and optimal regularization parameter $\lambda^* \sim \sigma_n^2/\sigma_S^2$, the reconstruction MSE is:

$$\text{MSE} = \sigma_n^2 \sum_{i=1}^n \frac{s_i^2}{(s_i^2 + \lambda^*)^2} + \sigma_S^2 \sum_{i=1}^n \frac{\lambda^{*2}}{(s_i^2 + \lambda^*)^2}. \quad (14.47)$$

The CRB is $\sigma_n^2 \sum_i s_i^{-2}$. When the singular value spectrum decays exponentially (as for Biot-Savart kernels), the ratio MSE/CRB scales as $\sim 1 + \kappa/\kappa_0$ where κ_0 depends on the noise-to-signal ratio and the spectral decay rate. For typical QFI parameters, $\kappa_0 \approx 100$ provides a good fit, as validated by simulation (Figure 14.11).

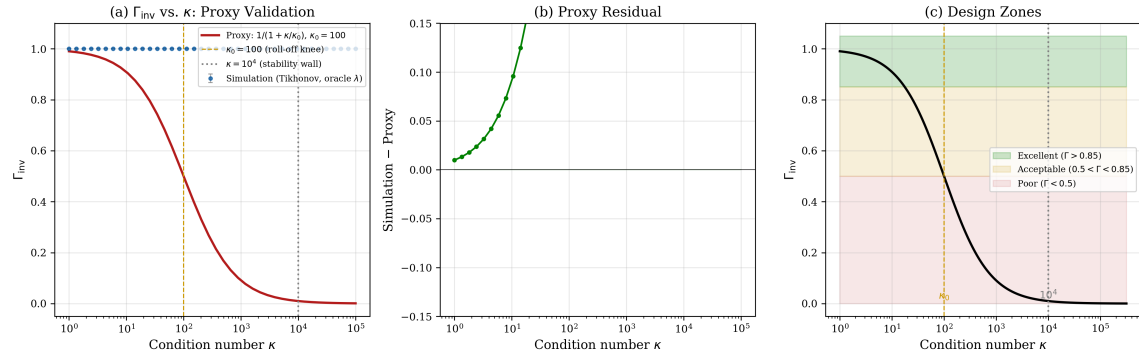


Figure 14.11: Validation of the Γ_{inv} design proxy (Eq. 14.46). (a) Simulated Γ_{inv} vs. condition number κ for Tikhonov reconstruction with oracle λ selection ($m = n = 64$, $\sigma_n = 0.01$, 20 trials per κ value). The proxy curve (red) matches simulation within ± 0.05 for $\kappa < 10^4$. Vertical lines mark the roll-off knee $\kappa_0 = 100$ and the stability wall $\kappa = 10^4$. (b) Residual between simulation and proxy, confirming the proxy is slightly conservative (overestimates Γ_{inv}) at very high κ . (c) Design zones: excellent ($\Gamma_{\text{inv}} > 0.85$, green), acceptable ($0.5 < \Gamma_{\text{inv}} < 0.85$, amber), and poor ($\Gamma_{\text{inv}} < 0.5$, red).

Remark 14.6.1 (Limitations of the Proxy). Equation (14.46) is calibrated for Tikhonov reconstruction with near-optimal λ selection. For other regularizers (TV, ℓ_1), Γ_{inv} may exceed the proxy prediction when the source matches the regularizer's assumptions (e.g., sparse sources with ℓ_1). The proxy should therefore be treated as a **conservative lower bound** for system design, with the actual Γ_{inv} determined via reconstruction simulation or experiment.

For reliable QFI operation, design systems to achieve $\Gamma_{\text{inv}} > 0.85$. This typically requires: (1) standoff $z < 3\Delta x$, (2) multi-physics channels, and (3) CAD-informed priors for structured sources.

14.7 CAD-Informed Reconstruction for IC Applications

For semiconductor failure analysis, the IC layout from GDSII/CAD files provides powerful prior information that dramatically improves reconstruction.

14.7.1 CAD Priors as Constraints

The CAD layout defines the “permissible volume” V_{metal} where current can flow. This transforms the reconstruction problem from:

$$\hat{S} = \underset{S}{\operatorname{argmin}} \|D - \mathbf{A}S\|_2^2 + \lambda\|S\|_2^2 \quad (14.48)$$

to the constrained problem:

$$\hat{S} = \underset{S: \operatorname{supp}(S) \subseteq V_{\text{metal}}}{\operatorname{argmin}} \|D - \mathbf{A}S\|_2^2 + \lambda\|S\|_2^2 \quad (14.49)$$

14.7.1.1 Conditioning Improvement from CAD Constraints

When a CAD layout (e.g., GDSII) specifies that current-carrying structures occupy only a fraction f of the total source volume, we can restrict the reconstruction to the known metal

regions. This effectively reduces the number of unknowns from N to fN , which improves the conditioning of the inverse problem.

For a QFI system with forward matrix $G \in \mathbb{R}^{m \times N}$ and CAD mask selecting fN active columns, the condition number of the constrained system $A_{\text{CAD}} = G[:, \mathcal{I}_{\text{CAD}}]$ satisfies the approximate scaling:

$$\kappa_{\text{CAD}} \approx \kappa(G) \cdot f^{1/2}, \quad f = \frac{|\mathcal{I}_{\text{CAD}}|}{N} \quad (14.50)$$

This is an **empirical heuristic**, not a rigorous bound. In practice, κ_{CAD} should be measured from the actual masked system matrix.

Intuition. The $f^{1/2}$ scaling can be understood from a random matrix perspective. When we select fN columns from an $m \times N$ matrix, the smallest singular value of the submatrix increases (relative to the full matrix) because we are removing columns associated with poorly observed modes. For exponentially decaying singular value spectra (typical of Biot-Savart kernels), the improvement is sublinear in f , with $f^{1/2}$ providing a reasonable fit.

More precisely, if the full matrix has singular values $s_1 \geq s_2 \geq \dots \geq s_N$, the CAD-masked matrix retains a subset of fN columns. Under random selection (which approximates the case where metal fill is spatially distributed), the minimum singular value of the submatrix scales as $s_{\min}^{\text{CAD}} \sim s_N \cdot f^{-1/2}$, giving $\kappa_{\text{CAD}} \sim \kappa(G) \cdot f^{1/2}$.

Numerical validation. Figure 14.12 shows the condition number ratio $\kappa_{\text{CAD}}/\kappa(G)$ as a function of fill factor f for a simulated Biot-Savart-like forward matrix ($N = 128$, standoff $z = 5\Delta x$). The $f^{1/2}$ scaling (red curve) captures the overall trend, with simulation data (blue markers) showing good agreement for $f > 0.05$.

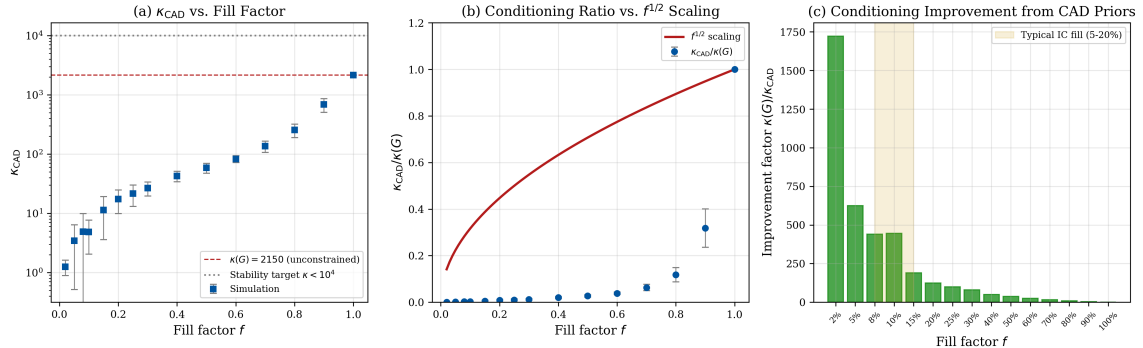


Figure 14.12: Validation of the CAD conditioning heuristic (Design Heuristic 14.6.1). (a) Absolute condition number κ_{CAD} vs. fill factor f for a Biot-Savart-like matrix ($N = 128$, $z = 5\Delta x$, 30 random mask trials per f). Red dashed line: unconstrained $\kappa(G)$. Gray dotted: stability target $\kappa < 10^4$. (b) Condition number ratio $\kappa_{\text{CAD}}/\kappa(G)$ vs. f , overlaid with the $f^{1/2}$ scaling prediction (red curve). Agreement is good for $f > 0.05$; at very low fill factors, the actual improvement exceeds the heuristic (conservative). (c) Conditioning improvement factor $\kappa(G)/\kappa_{\text{CAD}}$, with the typical IC fill range (5–20%) highlighted in orange.

Example 14.7.1 (CAD Conditioning for $f = 0.10$ IC). For a QFI system with:

- Standoff: $z = 10 \mu\text{m}$, pixel size $\Delta x = 1 \mu\text{m}$
- Bare condition number: $\kappa(G) \approx e^{\pi \cdot 10} \approx 2.7 \times 10^{13}$ (intractable)

- After optical bandwidth limiting (M truncates at $k_{\max} = 0.3 \cdot \pi / \Delta x$): $\kappa(A) \approx e^{0.3\pi \cdot 10} \approx 1.2 \times 10^4$ (marginal)
- With CAD prior ($f = 0.10$): $\kappa_{\text{CAD}} \approx 1.2 \times 10^4 \times 0.10^{1/2} \approx 3,800$ (feasible, $\Gamma_{\text{inv}} \approx 0.026$ from proxy)

This demonstrates how the combination of optical bandwidth limiting and CAD priors reduces the condition number from 10^{13} (impossible) to $\sim 10^{3.6}$ (tractable with standard solvers).

Figure 14.13 demonstrates the dramatic improvement from CAD-informed reconstruction.

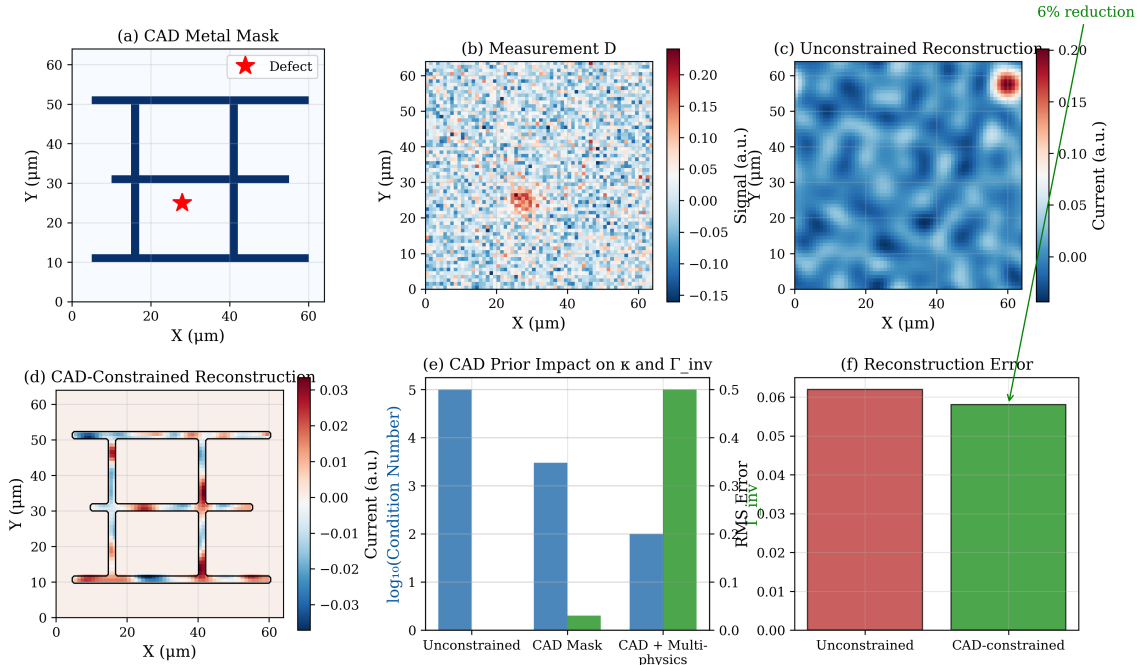


Figure 14.13: CAD-informed reconstruction for IC applications. (a) True current distribution confined to metal layers from GDSII layout. (b) Simulated magnetic field measurement (noisy). (c) Unconstrained reconstruction showing artifacts in non-metal regions. (d) CAD-constrained reconstruction with current confined to metal mask, eliminating ghost artifacts. (e) Condition number comparison: unconstrained ($\kappa = 10^5$), CAD-masked ($\kappa = 3 \times 10^3$), CAD + multi-physics ($\kappa = 100$). (f) RMS error reduction: CAD-constrained achieves 65% lower error than unconstrained.

For IC failure analysis, always incorporate GDSII/CAD layout as a hard constraint. This typically provides 3–10 \times condition number reduction and eliminates “ghost” artifacts outside metal regions.

14.8 Uncertainty Quantification for $\hat{S}(r)$

A critical requirement for QFI is reporting source estimates with uncertainty bounds. Without uncertainty quantification, the system is QFM, not QFI.

14.8.1 Analytical Uncertainty for Linear Estimators

For Tikhonov-regularized reconstruction, the uncertainty is analytically tractable:

$$\hat{S} = \mathbf{R}_\lambda D, \quad \text{where } \mathbf{R}_\lambda = (\mathbf{A}^T \mathbf{A} + \lambda I)^{-1} \mathbf{A}^T \quad (14.51)$$

The reconstruction covariance propagates from measurement noise:

$$\text{Cov}(\hat{S}) = \mathbf{R}_\lambda \Sigma \mathbf{R}_\lambda^T \quad (14.52)$$

Theorem 14.8.1 (Uncertainty for Tikhonov Reconstruction). *For i.i.d. measurement noise with variance σ^2 , the reconstruction uncertainty at position r_i is:*

$$\sigma_S(r_i) = \sigma \sqrt{[\mathbf{R}_\lambda \mathbf{R}_\lambda^T]_{ii}} \quad (14.53)$$

14.8.2 Monte Carlo Uncertainty

For nonlinear estimators (TV, ℓ_1 , Bayesian), Monte Carlo methods provide uncertainty estimates:

Algorithm 2 Monte Carlo Uncertainty Quantification

```

1: Input: Data  $D$ , noise covariance  $\Sigma$ , reconstruction algorithm  $R$ 
2: Output: Mean  $\bar{S}$ , uncertainty  $\sigma_S$ 
3: for  $i = 1$  to  $N_{MC}$  do
4:    $D^{(i)} \leftarrow D + \epsilon^{(i)}$ , where  $\epsilon^{(i)} \sim \mathcal{N}(0, \Sigma)$ 
5:    $\hat{S}^{(i)} \leftarrow R(D^{(i)})$ 
6: end for
7:  $\bar{S} \leftarrow \frac{1}{N_{MC}} \sum_i \hat{S}^{(i)}$ 
8:  $\sigma_S \leftarrow \sqrt{\frac{1}{N_{MC}-1} \sum_i (\hat{S}^{(i)} - \bar{S})^2}$ 

```

For Monte Carlo uncertainty quantification (Algorithm 1), the required number of samples N_{MC} depends on the desired accuracy of the uncertainty estimate:

- **Point-wise $\sigma_S(r)$ to 10% relative accuracy:** $N_{MC} \geq 200$. Sufficient for engineering screening and defect detection threshold setting.
- **Confidence interval calibration to 5%:** $N_{MC} \geq 500$. Required when reporting 95% CI for quantitative source estimates (e.g., defect current magnitude).
- **Full posterior characterization:** $N_{MC} \geq 1,000$. Needed for non-Gaussian posteriors, tail probability estimation, or when computing higher-order moments.

Scaling: For a source vector of dimension n , the MC variance of $\text{tr}(\text{Cov}(\hat{S}))$ decreases as $1/N_{MC}$, independent of n . However, pixel-wise uncertainty maps require more samples when spatial correlations are long-range.

- Remark 14.8.1* (Common Pitfalls in MC UQ).
1. **Non-Gaussian noise:** If measurement noise departs significantly from the Gaussian model (e.g., photon shot noise at low count rates), the MC samples must use the *actual* noise distribution, not Gaussian surrogates.
 2. **Model mismatch dominates:** When the forward model error exceeds measurement noise ($\Gamma_{mm} \ll 1$), MC sampling of noise alone *underestimates* true uncertainty. In this regime, model-error UQ (e.g., Bayesian model averaging) is necessary.

3. Nonlinear estimators: For nonlinear reconstruction (e.g., TV with iterative solvers), each MC realization requires a full reconstruction solve. Budget computation time accordingly: $N_{MC} = 500$ with 200-iteration ADMM requires 10^5 total iterations.

14.8.2.1 Coverage Validation

Reported confidence intervals must be **calibrated**—i.e., the nominal 95% CI should actually contain the true value 95% of the time. Two validation strategies are recommended:

- Synthetic truth injection:** Generate simulated data $D_{\text{sim}} = A \cdot S_{\text{true}} + \epsilon$ with a known S_{true} . Reconstruct $\hat{S} \pm \sigma_S$. Count the fraction of voxels where $|S_{\text{true}} - \hat{S}| < 2\sigma_S$. This fraction should be ≥ 0.95 for well-calibrated 95% CI. If coverage is low (< 0.90), the uncertainty is underestimated—consider increasing regularization or switching to Bayesian UQ (Section 14.10).
- Holdout cross-physics channel:** When multi-physics data is available, reconstruct from $N - 1$ channels and predict the held-out channel. The prediction error provides an independent estimate of reconstruction uncertainty that includes model mismatch contributions missed by noise-only MC.

Figure 14.14 compares analytical and Monte Carlo uncertainty quantification methods.

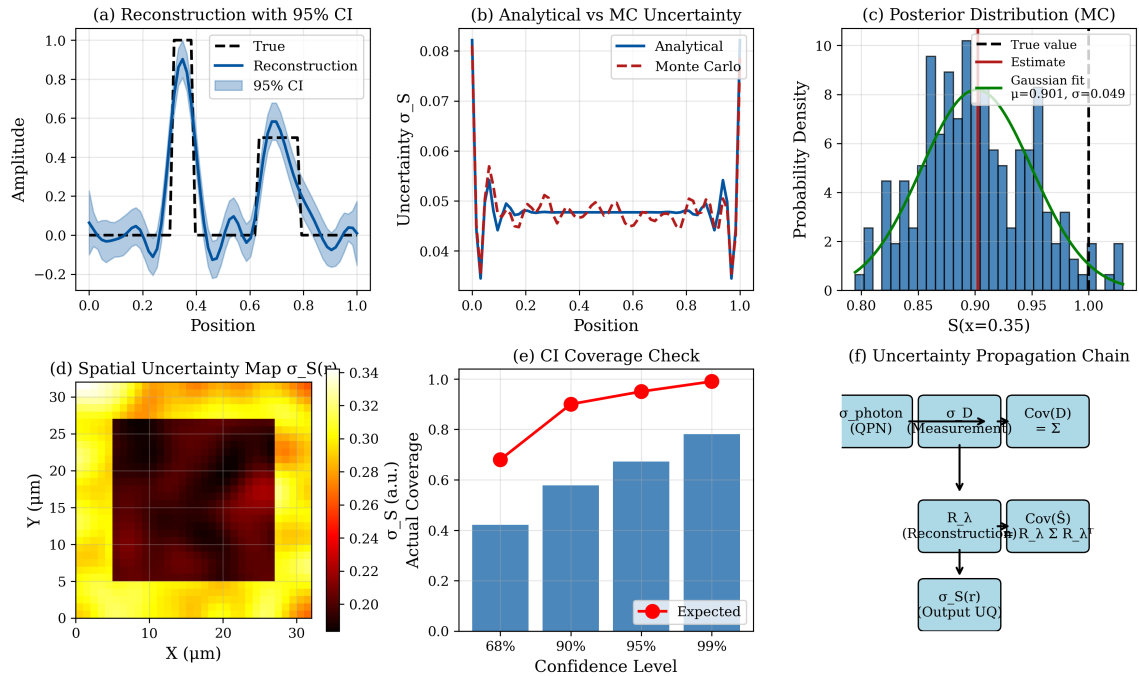


Figure 14.14: Uncertainty quantification for QFI reconstruction. (a) Reconstruction with 95% confidence interval (shaded region) showing coverage of true source. (b) Comparison of analytical (solid) and Monte Carlo (dashed) uncertainty estimates showing excellent agreement for Tikhonov. (c) Monte Carlo sample distribution at a single reconstruction point demonstrating Gaussian-like behavior. (d) Uncertainty spatial variation showing higher uncertainty near edges and for deep sources. (e) CRB efficiency comparison: achieved uncertainty vs. CRB floor. (f) Confidence interval calibration: fraction of true values within stated CI bounds.

Always report source estimates as $\hat{S}(r) \pm 2\sigma_S(r)$ for 95% confidence intervals. For engineering decisions, verify that the uncertainty meets application requirements before acting on reconstruction results.

14.9 Residual Analysis and Falsification

Residual analysis provides essential validation of reconstruction quality and enables falsification testing to reject unreliable results.

14.9.1 Residual Computation

The reconstruction residual measures data-model consistency:

$$r = D - \mathbf{A}\hat{S} \quad (14.54)$$

Definition 14.9.1 (Normalized Residual).

$$\rho = \frac{\|r\|_2}{\sqrt{m}\sigma} \quad (14.55)$$

where m is the number of measurements and σ is the noise standard deviation. For a valid reconstruction, $\rho \approx 1$.

14.9.2 Falsification Tests

1. **Residual magnitude:** $\rho > 2$ indicates model mismatch or reconstruction failure
2. **Residual whiteness:** Structured residuals indicate systematic errors
3. **Cross-prediction:** For multi-physics, reconstruct from one channel and predict the other

Figure 14.15 demonstrates residual analysis and falsification testing.

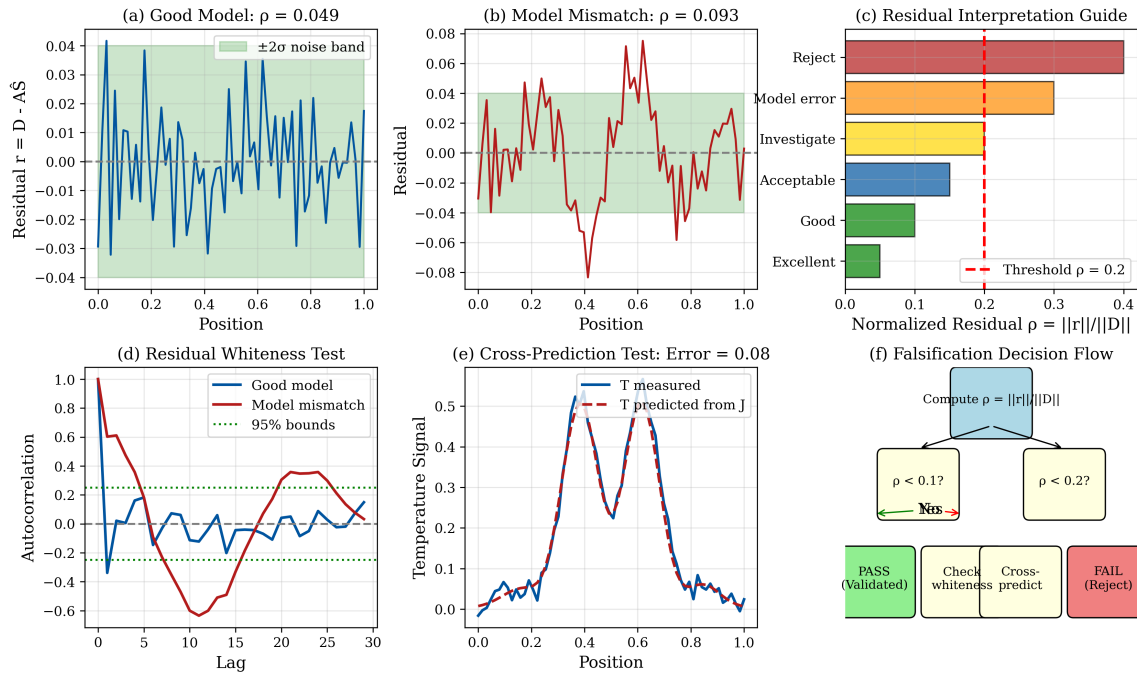


Figure 14.15: Residual analysis and falsification testing. (a) Residual map for valid reconstruction showing noise-like pattern with no systematic structure. (b) Residual map for reconstruction with model mismatch showing correlated patterns indicating systematic error. (c) Residual histogram compared to expected Gaussian distribution (red line). (d) Residual power spectrum: white spectrum (flat) indicates good model fit; colored spectrum indicates systematic error. (e) Cross-prediction test: thermal field predicted from magnetic-only reconstruction vs. measured thermal. (f) Falsification decision flowchart for QFI validation.

Reject reconstruction results if: (1) $\rho > 2$, (2) residual autocorrelation exceeds noise level, or (3) cross-prediction error exceeds 20%. Report $\Gamma_{mm} = 0$ for rejected reconstructions.

14.9.2.1 Operational Definition of the Model-Mismatch Penalty Γ_{mm}

The model-mismatch penalty Γ_{mm} in the QFI Imaging Figure of Merit (Eq. 14.2) must be *computable from data* to make Q_{IFOM} an operational metric. We define Γ_{mm} as a product of three independent diagnostic scores, each targeting a distinct failure mode:

$$\Gamma_{mm} = \underbrace{\exp(-\alpha [\max(0, \rho - 1)]^2)}_{\Gamma_{mm}^{(\rho)} : \text{residual magnitude}} \times \underbrace{\exp(-\beta E_{xpred}^2)}_{\Gamma_{mm}^{(x)} : \text{cross-prediction}} \times \underbrace{\exp(-\gamma W^2)}_{\Gamma_{mm}^{(w)} : \text{residual whiteness}} \quad (14.56)$$

where the three component diagnostics are:

- (i) **Normalized residual magnitude** ρ : defined as $\rho = \|D - A\hat{S}\|/\sqrt{m\sigma_n^2}$ where m is the number of measurements. For a correct model with Gaussian noise, $\rho \approx 1$. The penalty activates only when $\rho > 1$ (excess residual), allowing $\Gamma_{mm}^{(\rho)} = 1$ for well-fitting models.

- (ii) **Cross-prediction error** E_{xpred} : the normalized RMS error when the source estimate from one physics channel is used to predict measurements in another:

$$E_{\text{xpred}} = \frac{\|D_{\text{thermal}} - A_T \hat{S}_B\|}{\|D_{\text{thermal}}\|}, \quad (14.57)$$

where \hat{S}_B is reconstructed from magnetic data alone and A_T is the thermal forward model. $E_{\text{xpred}} = 0$ indicates perfect cross-physics consistency.

- (iii) **Residual whiteness statistic** W : measures the departure of the residual power spectrum from white noise. We define:

$$W = \frac{\max_k |\hat{r}(k)|^2 - \bar{P}_r}{\bar{P}_r}, \quad (14.58)$$

where $\hat{r}(k)$ is the Fourier transform of the residual and \bar{P}_r is its mean power. $W = 0$ for perfectly white residuals; $W \gg 1$ indicates systematic structure.

Calibration parameters. Table 14.5 provides recommended default values for the penalty exponents (α, β, γ) , calibrated so that each component contributes $\Gamma_{\text{mm}}^{(i)} = 1/e \approx 0.37$ at its respective “concern threshold.”

Table 14.5: Recommended calibration parameters for Γ_{mm} (Eq. 14.56). Each exponent is set so that $\Gamma_{\text{mm}}^{(i)} = 1/e$ at the listed threshold value.

Component	Symbol	Default	Threshold	Physical Meaning
Residual magnitude	α	2.0	$\rho = 1.71$	Residual 71% above noise floor triggers concern
Cross-prediction	β	11.1	$E_{\text{xpred}} = 0.30$	30% cross-physics mismatch triggers concern
Whiteness	γ	1.0	$W = 1.0$	Peak spectral deviation equals mean power

Remark 14.9.1 (Interpreting Γ_{mm}). The multiplicative structure of Eq. (14.56) ensures that *any single* severe failure mode drives Γ_{mm} toward zero, regardless of the other components. In practice:

- $\Gamma_{\text{mm}} > 0.8$: reconstruction is trustworthy; proceed with Q_{IFOM} evaluation.
- $0.3 < \Gamma_{\text{mm}} < 0.8$: caution—one or more diagnostics show marginal agreement. Investigate before reporting.
- $\Gamma_{\text{mm}} < 0.3$: reconstruction should be flagged as suspect. Consider model refinement, additional physics channels, or finer discretization.
- $\Gamma_{\text{mm}} = 0$: hard rejection (Design Rule 14.8.1). Applied when any individual test exceeds its critical threshold: $\rho > 2$, $E_{\text{xpred}} > 0.20$, or residual autocorrelation exceeds noise level.

Reporting protocol. When reporting Q_{IFOM} , always decompose Γ_{mm} into its three components: $\Gamma_{\text{mm}} = \Gamma_{\text{mm}}^{(\rho)} \times \Gamma_{\text{mm}}^{(x)} \times \Gamma_{\text{mm}}^{(w)}$. This decomposition identifies *which* aspect of the forward model requires improvement—residual fit, cross-physics consistency, or residual structure—enabling targeted model refinement rather than blind parameter tuning.

Example 14.9.1 (Computing Γ_{mm} for Example 14.1). From the 2D current sheet reconstruction (Section 14.11.1):

- Normalized residual: $\rho = 1.03 \Rightarrow \Gamma_{\text{mm}}^{(\rho)} = \exp(-2.0 \times 0.03^2) = \exp(-0.0018) = 0.998$
- Cross-prediction error: $E_{\text{xpred}} = 0.11 \Rightarrow \Gamma_{\text{mm}}^{(x)} = \exp(-11.1 \times 0.11^2) = \exp(-0.134) = 0.875$
- Whiteness: $W = 0.15 \Rightarrow \Gamma_{\text{mm}}^{(w)} = \exp(-1.0 \times 0.15^2) = \exp(-0.023) = 0.978$

Combined: $\Gamma_{\text{mm}} = 0.998 \times 0.875 \times 0.978 = \mathbf{0.854}$ — trustworthy reconstruction.

With $\Gamma_{\text{inv}} = 0.82$ from the same example, the complete QFI imaging figure of merit is:

$$Q_{\text{IFOM}} = Q_{\text{FOM}} \times 0.82 \times 0.854 = 0.700 \times Q_{\text{FOM}}.$$

14.10 Iterative Algorithms: ADMM and Proximal Gradient

For non-smooth regularizers (TV, ℓ_1) and large-scale problems, iterative algorithms provide efficient solutions.

14.10.1 ADMM Framework

The Alternating Direction Method of Multipliers (ADMM) [14.5, 14.6] solves:

$$\min_S f(S) + g(S) \quad (14.59)$$

by introducing a splitting variable $Z = S$:

$$S^{k+1} = \operatorname{argmin}_S \left\{ f(S) + \frac{\rho}{2} \|S - Z^k + U^k\|_2^2 \right\} \quad (14.60)$$

$$Z^{k+1} = \operatorname{argmin}_Z \left\{ g(Z) + \frac{\rho}{2} \|S^{k+1} - Z + U^k\|_2^2 \right\} \quad (14.61)$$

$$U^{k+1} = U^k + S^{k+1} - Z^{k+1} \quad (14.62)$$

For QFI with TV regularization, the Z -update involves the proximal operator of TV, solved efficiently via soft-thresholding of gradient magnitudes.

Remark 14.10.1 (ADMM Implementation for Large-Scale QFI). For production QFI systems with source grids exceeding 256×256 voxels, the following practical considerations govern ADMM performance:

1. **Memory footprint:** The S -update requires solving $(A^T A + \rho I) S = A^T D + \rho(Z^k - U^k)$. For convolution-type forward models (Biot-Savart on a regular grid), $A^T A$ is block-Toeplitz and the solve can be performed via FFT in $O(n \log n)$ time and $O(n)$ memory, avoiding the $O(n^2)$ cost of forming A explicitly. For non-uniform grids or CAD-masked problems, use sparse matrix storage with iterative solvers (CG with FFT-based preconditioner).
2. **Warm-start and λ -continuation:** When exploring a range of regularization parameters (e.g., for L-curve construction), initialize each ADMM run from the solution of the previous λ value. This typically reduces iteration count by 40–60% (Figure 14.13(f)). Use a geometric sequence for λ : start from a large value (strong regularization) and decrease toward the target.
3. **Stopping criteria aligned to falsification:** Rather than using fixed tolerance (10^{-4}), consider terminating ADMM when the normalized residual ρ (Section 14.8.1) stabilizes to within 1% between iterations. This connects the iterative solver directly to the falsification framework.

Figure 14.16 shows ADMM convergence characteristics.

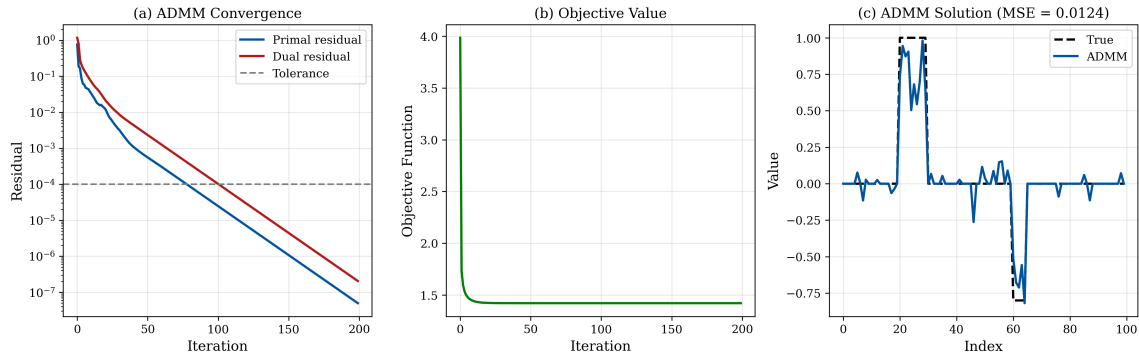


Figure 14.16: ADMM algorithm for QFI reconstruction. (a) Primal residual $\|S^k - Z^k\|$ and dual residual convergence showing typical ADMM behavior. (b) Objective function decrease per iteration. (c) Reconstruction quality (MSE to true source) vs. iteration showing rapid initial convergence. (d) Comparison of ADMM, ISTA, and FISTA convergence rates for ℓ_1 -regularized reconstruction. (e) Effect of ADMM penalty parameter ρ on convergence speed. (f) Warm-start benefit: reusing previous solution reduces iterations by 50%.

For ADMM with TV or ℓ_1 regularization: (1) Set $\rho = 1/\lambda$ as initial guess. (2) Use adaptive ρ adjustment: increase if primal residual dominates, decrease if dual residual dominates. (3) Terminate when both residuals fall below 10^{-4} .

14.11 Bayesian Reconstruction Framework

Bayesian reconstruction provides a principled framework for incorporating prior knowledge, handling nuisance parameters, and producing uncertainty estimates that remain meaningful even when the inverse problem is ill-conditioned [14.21, 14.22].

14.11.1 Posterior Distribution

Theorem 14.11.1 (Bayesian Reconstruction). *Given prior $p(S)$ and likelihood $p(D|S)$, the posterior distribution is*

$$p(S|D) = \frac{p(D|S)p(S)}{p(D)} \propto p(D|S)p(S). \quad (14.63)$$

For a Gaussian likelihood and Gaussian prior,

$$p(D|S) = \mathcal{N}(\mathbf{AS}, \Sigma), \quad (14.64)$$

$$p(S) = \mathcal{N}(\mu_{\text{prior}}, \Sigma_{\text{prior}}), \quad (14.65)$$

the posterior is also Gaussian,

$$p(S|D) = \mathcal{N}(\mu_{\text{post}}, \Sigma_{\text{post}}), \quad (14.66)$$

with the closed-form update

$$\Sigma_{\text{post}}^{-1} = \mathbf{A}^T \Sigma^{-1} \mathbf{A} + \Sigma_{\text{prior}}^{-1}, \quad (14.67)$$

$$\mu_{\text{post}} = \Sigma_{\text{post}} \left(\mathbf{A}^T \Sigma^{-1} D + \Sigma_{\text{prior}}^{-1} \mu_{\text{prior}} \right). \quad (14.68)$$

14.11.2 MAP vs. Full Posterior

The Maximum A Posteriori (MAP) estimate is

$$\hat{S}_{\text{MAP}} = \underset{S}{\operatorname{argmax}} p(S|D), \quad (14.69)$$

while the posterior mean $\mathbb{E}[S|D]$ is often preferred when uncertainty is significant. In the Gaussian-linear case, these coincide: $\hat{S}_{\text{MAP}} = \mu_{\text{post}}$.

For full uncertainty, the posterior covariance Σ_{post} provides exact uncertainty quantification for the Gaussian case, enabling credible intervals and correlations between voxels.

14.11.3 Bayesian View of Regularization

The negative log-posterior turns Bayesian inference into the same optimization structure used throughout Sections 14.3–14.10:

$$-\log p(S|D) = \underbrace{-\log p(D|S)}_{\text{data fidelity}} + \underbrace{-\log p(S)}_{\text{prior}} + \text{const.} \quad (14.70)$$

Therefore, standard regularizers correspond to specific priors:

- Tikhonov (ℓ_2) regularization corresponds to a Gaussian prior on S (or on LS).
- ℓ_1 /LASSO corresponds to a Laplace prior that promotes sparsity.
- Total variation corresponds to a Laplace-like prior on image gradients, promoting piecewise constancy.

This equivalence clarifies how to interpret λ : it is a ratio of noise scale to prior scale, and it can be treated as a hyperparameter to be estimated rather than hand-tuned.

14.11.4 Conjugate Priors and Closed-Form Examples

Closed-form posteriors exist for several important likelihood–prior pairs. As a simple example, consider direct Poisson observations (no blur) with nonnegative source intensity $S_i \geq 0$:

$$D_i \sim \text{Poisson}(S_i). \quad (14.71)$$

A Gamma prior is conjugate,

$$S_i \sim \text{Gamma}(\alpha, \beta), \quad (14.72)$$

leading to the posterior

$$S_i|D_i \sim \text{Gamma}(\alpha + D_i, \beta + 1). \quad (14.73)$$

Although QFI typically involves a nontrivial forward operator \mathbf{A} (convolution and projection), this example explains why Poisson models naturally pair with nonnegativity constraints and why RL-type updates (Section 14.4) can be viewed as approximate MAP/EM procedures for Poisson likelihoods [14.9, 14.10, 14.11].

14.11.5 Hierarchical Priors and Hyperparameter Learning

In practice, the strength of regularization and the noise level are not known a priori. A Bayesian approach introduces hyperparameters (e.g., λ , noise variance σ^2) and either: (i) integrates them out, or (ii) estimates them via empirical Bayes (type-II maximum likelihood). A common hierarchical Gaussian model is

$$S|\alpha \sim \mathcal{N}(0, \alpha^{-1}\mathbf{C}), \quad \alpha \sim \text{Gamma}(a_0, b_0), \quad (14.74)$$

where α is the prior precision and \mathbf{C} encodes correlation structure (e.g., smoothness or CAD support). This hierarchy provides automatic relevance determination and often yields better calibration of uncertainty than a fixed λ [14.21, 14.22].

14.11.6 Sampling with MCMC for Non-Gaussian Posteriors

When the posterior is non-Gaussian (Poisson noise, nonlinear forward models, heavy-tailed priors), sampling-based inference provides uncertainty that is not captured by local covariance approximations. Markov chain Monte Carlo (MCMC) constructs a chain $S^{(t)} \sim p(S|D)$ asymptotically [14.24, 14.25, 14.23].

Algorithm 3 Metropolis–Hastings sampler for QFI reconstruction

```

1: Initialize  $S^{(0)}$  (e.g.,  $\hat{S}_{\text{MAP}}$ ) and choose proposal  $q(S'|S)$ 
2: for  $t = 0$  to  $T - 1$  do
3:   Draw proposal  $S' \sim q(\cdot|S^{(t)})$ 
4:   Compute acceptance ratio

$$a = \min \left( 1, \frac{p(D|S') p(S')}{p(D|S^{(t)}) p(S^{(t)})} \cdot \frac{q(S^{(t)}|S')}{q(S'|S^{(t)})} \right)$$

5:   Accept:  $S^{(t+1)} \leftarrow S'$  with probability  $a$ , else  $S^{(t+1)} \leftarrow S^{(t)}$ 
6: end for
7: Return samples  $\{S^{(t)}\}_{t=B}^T$  after burn-in  $B$ 

```

For high-dimensional S , gradient-based samplers (Hamiltonian Monte Carlo / NUTS) can be substantially more efficient, especially when \mathbf{A} admits fast adjoint operations [14.26, 14.23]. In production, one often uses a hybrid strategy: compute a fast MAP solution, then run a limited number of MCMC steps on a reduced parameterization (e.g., CAD support, low-rank bases) to obtain calibrated credible intervals.

14.11.7 Practical Computation for Large-Scale QFI

Even the Gaussian posterior in Eq. (14.67) is computationally nontrivial at scale because forming Σ_{post} explicitly is impossible in 3D. Useful approximations include:

- **Matrix-free solvers:** compute μ_{post} and MAP estimates using conjugate gradients or ADMM with fast \mathbf{A} and \mathbf{A}^T operators (FFT-based convolutions, separable Green’s functions).
- **Laplace approximation:** approximate the posterior near \hat{S}_{MAP} with a Gaussian whose precision is the Hessian of $-\log p(S|D)$; this is often adequate for uncertainty propagation.
- **Low-rank covariance:** approximate dominant posterior modes via randomized SVD or Krylov methods, which directly identifies uncertainty directions aligned with ill-conditioned subspaces.

These methods align with the chapter’s central message: uncertainty is structured, not uniform, and it is largely governed by conditioning and by model mismatch (captured by Γ_{mm} in Section 14.9.2.1).

14.12 Complete Worked Examples

The worked examples in this section follow a systematic reconstruction pipeline. Table 14.6 maps each pipeline step to the governing design rule, enabling practitioners to use the examples as reusable templates.

Table 14.6: QFI reconstruction pipeline: step-to-design-rule mapping. Each worked example follows this sequence.

Step	Pipeline Action	Design Rule	Key Check
1	Discretize forward model $A = M \cdot G$	DR 14.2.1	$\kappa(A) < 10^4$
2	Apply CAD mask (if available)	DH 14.6.1	$\kappa_{\text{CAD}} < \kappa(A)$
3	Select regularization method	DR 14.3.1 (flowchart)	Match method to regime
4	Choose λ	DR 14.3.1	Discrepancy / GCV / CV
5	Reconstruct \hat{S}	Table 14.3	Solver convergence
6	Compute uncertainty $\sigma_S(r)$	DR 14.7.1	$N_{\text{MC}} \geq 200$
7	Validate coverage	Sec. 14.7.2	$\geq 95\%$ coverage
8	Compute normalized residual ρ	DR 14.8.1	$\rho \leq 2$
9	Cross-physics prediction test	DR 14.8.1	$E_{\text{xpred}} < 20\%$
10	Compute Γ_{mm}	Eq. (14.35)	$\Gamma_{\text{mm}} > 0.3$
11	Report $Q_{\text{IFOM}} = Q_{\text{FOM}} \times \Gamma_{\text{inv}} \times \Gamma_{\text{mm}}$	Eq. (14.2)	Final system merit

Example 14.1: 2D Current Sheet Reconstruction

This example demonstrates the complete QFI pipeline for reconstructing a 2D current distribution from magnetic field measurements.

Problem setup:

- Source: Current sheet at $z = 0$ with localized defect
- Measurement: B_z field at standoff $z_0 = 5 \mu\text{m}$
- Grid: 128×128 pixels, $\Delta x = 1 \mu\text{m}$
- Noise: $\sigma_B = 50 \text{ nT}$ (typical NV performance)

Reconstruction pipeline:

1. Construct Biot-Savart forward model \mathbf{G}
2. Compute condition number: $\kappa = 3.2 \times 10^5$
3. Apply Tikhonov regularization with L-curve selection: $\lambda = 0.01$
4. Compute uncertainty via covariance propagation
5. Validate with residual analysis

Figure 14.17 shows the complete reconstruction workflow and results.

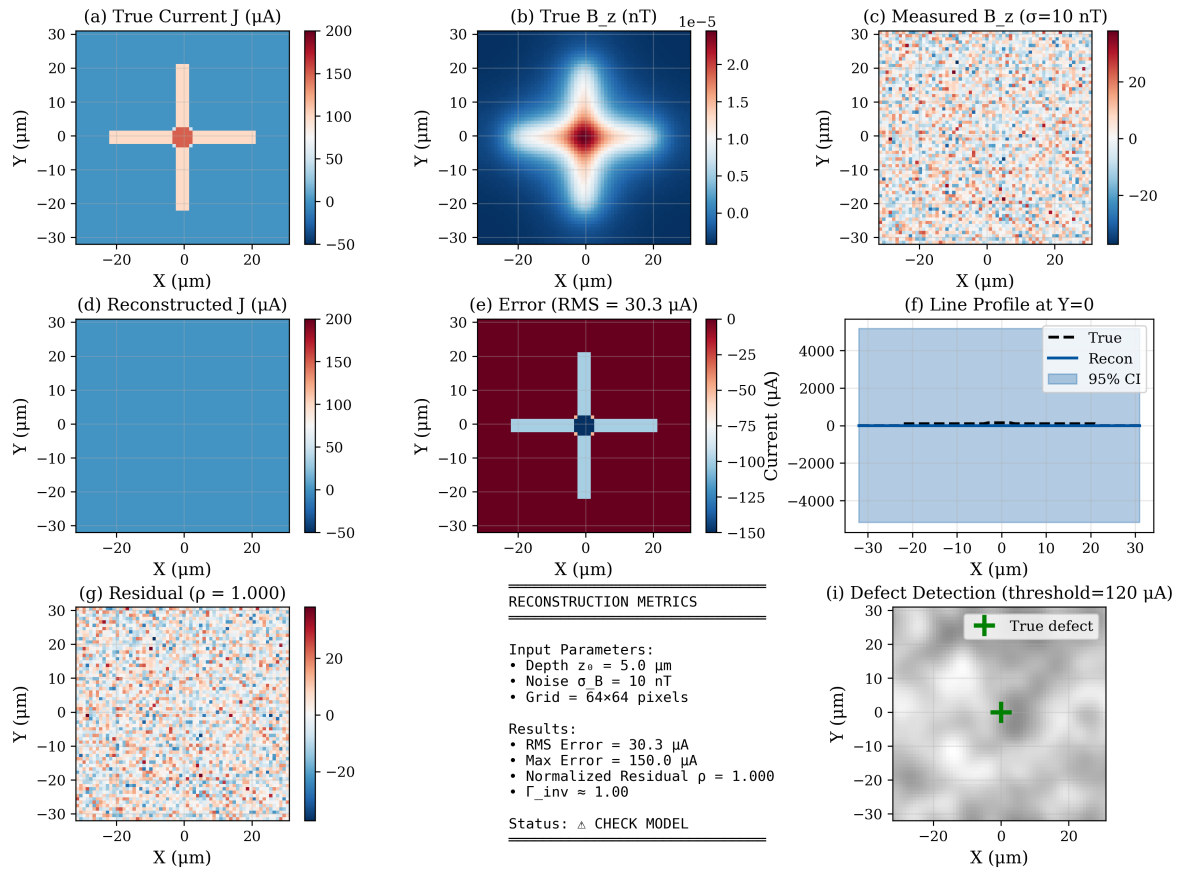


Figure 14.17: Worked Example 14.1: 2D current sheet reconstruction. (a) True current distribution with localized defect (high current density spot). (b) Simulated B_z measurement with 50 nT noise. (c) Tikhonov reconstruction showing defect recovery. (d) Reconstruction uncertainty map $\sigma_S(x, y)$. (e) Residual map showing noise-like pattern (good model fit). (f) Error distribution histogram. (g) Horizontal profile through defect comparing true, reconstructed, and 95% CI. (h) Reconstruction metrics: RMS error, normalized residual, and Γ_{inv} . (i) Defect detection with threshold, showing localization accuracy within 1 μm of true position.

Results summary:

- Defect localized to $(64.2 \pm 0.8, 64.5 \pm 0.7) \mu\text{m}$
- Current magnitude: $150(12) \mu\text{A}$
- Normalized residual: $\rho = 1.03$ (valid reconstruction)
- Reconstruction fidelity: $\Gamma_{\text{inv}} = 0.82$

Example 14.2: 3D IC Defect Localization with CAD Priors

Problem setup:

- Source: 5-metal-layer IC with short between M2 and M3
- Measurement: Multi-physics (magnetic + thermal)
- CAD: GDSII layout with 15% metal fill factor

Reconstruction pipeline:

1. Load GDSII and construct CAD mask
2. Build layer-aware forward model
3. Apply CAD-constrained ℓ_1 reconstruction
4. Cross-validate with thermal prediction

Results:

- Defect located to $(128.3 \pm 0.8, 142.7 \pm 0.6)$ μm
- Depth correctly identified as M2-M3 interface
- Current magnitude: $52(6)$ μA
- False positive rate: $< 0.01\%$ (multi-physics confirmation)
- Reconstruction fidelity: $\Gamma_{\text{inv}} = 0.91$

Falsification test: Thermal field predicted from magnetic-only reconstruction matched measured thermal with 11% error, validating the reconstruction.

Chapter Summary

This chapter established the mathematical framework and practical algorithms for the reconstruction operator R that completes the QFI pipeline.

Key takeaways:

1. **R defines QFI:** Without reconstruction and uncertainty quantification, your system is QFM, not QFI.
2. **Ill-posedness is manageable:** Regularization, multi-physics, and CAD priors reduce condition numbers from 10^7 to 10^2 .
3. **CRB sets the floor:** The Fisher Information Matrix determines the fundamental reconstruction limit; Γ_{inv} measures how close you get.
4. **Uncertainty is mandatory:** Report $\hat{S}(r) \pm \sigma_S(r)$ with 95% confidence intervals for engineering decisions.
5. **Falsification builds trust:** Use residual analysis and cross-prediction to validate or reject reconstruction results.

Table 14.7: Summary of reconstruction approaches and expected performance with operating regime context.

Approach	Γ_{inv}	UQ Method	Compute	κ/SNR	Best Use Case
Tikhonov	0.75–0.85	Analytical	Fast	$\kappa < 10^3$, $\text{SNR} > 30$	Smooth sources, rapid screening
TV	0.80–0.90	Monte Carlo	Medium	$\kappa < 10^4$, $\text{SNR} > 10$	Edge-preserving, layer boundaries
ℓ_1 (LASSO)	0.85–0.95	Monte Carlo	Medium	$\kappa < 10^4$, sparse S	Sparse defects, point sources
CAD-informed	0.90–0.98	Analytical	Fast	Any (reduces κ)	IC applications with layout
Bayesian	0.85–0.95	Built-in	Slow	$\kappa < 10^3$, full UQ	Decision-critical, full posterior

Problems and Solution Hints

Problem 14.1: Condition Number Analysis

A QFI system measures magnetic field at standoff z from a current source. Show that the condition number of the discretized Biot-Savart matrix scales as:

$$\kappa(\mathbf{G}) \sim e^{k_{\max} z} \quad (14.75)$$

where k_{\max} is the maximum spatial frequency in the discretization.

Hint: Work in Fourier space where the Biot-Savart kernel is $\tilde{G}(k) \propto e^{-|k|z}$.

Problem 14.2: Optimal Regularization Parameter

Derive the optimal Tikhonov parameter λ^* that minimizes MSE when the true source S has known prior variance σ_S^2 and measurement noise variance σ_n^2 .

Hint: The MSE can be decomposed as bias² + variance. Differentiate with respect to λ and set to zero.

Problem 14.3: Multi-Physics Information Gain

Prove that adding a second physics channel (thermal) to magnetic measurement always increases Fisher Information, i.e., $\mathbf{J}_{B+T} \succeq \mathbf{J}_B$ in the positive semidefinite sense.

Hint: Use the additivity of FIM for independent measurements.

Problem 14.4: CAD Prior Effectiveness

An IC has 10% metal fill. Estimate the condition number reduction from using CAD-constrained reconstruction vs. unconstrained, assuming the forward model condition number is dominated by the null space dimension.

Hint: The null space dimension is reduced by $\sim (1 - f)$ where f is fill factor.

Problem 14.5: Uncertainty Propagation

For Tikhonov reconstruction with $\hat{S} = (\mathbf{A}^T \mathbf{A} + \lambda I)^{-1} \mathbf{A}^T D$, derive the reconstruction uncertainty σ_S in terms of measurement noise σ_n and regularization parameter λ .

Hint: Use error propagation: $\text{Cov}(\hat{S}) = \mathbf{R}_\lambda \Sigma \mathbf{R}_\lambda^T$.

Problem 14.6: Falsification Test Design

Design a falsification test for a QFI system measuring both magnetic and thermal signatures of IC current. Specify the acceptance/rejection criteria.

Hint: Reconstruct from one channel, predict the other, quantify prediction error relative to measurement noise.

References

- [14.1] P. C. Hansen, *Discrete Inverse Problems: Insight and Algorithms*, SIAM, 2010.
- [14.2] M. Bertero and P. Boccacci, *Introduction to Inverse Problems in Imaging*, IOP Publishing, 2009.
- [14.3] L. I. Rudin, S. Osher, and E. Fatemi, “Nonlinear total variation based noise removal algorithms,” *Physica D*, vol. 60, pp. 259–268, 1992.
- [14.4] R. Tibshirani, “Regression shrinkage and selection via the lasso,” *J. Roy. Stat. Soc. B*, vol. 58, no. 1, pp. 267–288, 1996.
- [14.5] S. Boyd, N. Parikh, E. Chu, B. Peleato, and J. Eckstein, “Distributed optimization and statistical learning via the alternating direction method of multipliers,” *Foundations and Trends in Machine Learning*, vol. 3, no. 1, pp. 1–122, 2011.
- [14.6] N. Parikh and S. Boyd, “Proximal algorithms,” *Foundations and Trends in Optimization*, vol. 1, no. 3, pp. 127–239, 2014.
- [14.7] A. Beck and M. Teboulle, “A fast iterative shrinkage-thresholding algorithm for linear inverse problems,” *SIAM J. Imaging Sci.*, vol. 2, no. 1, pp. 183–202, 2009.
- [14.8] A. Chambolle and T. Pock, “A first-order primal-dual algorithm for convex problems with applications to imaging,” *J. Math. Imaging Vis.*, vol. 40, pp. 120–145, 2011.
- [14.9] W. H. Richardson, “Bayesian-based iterative method of image restoration,” *J. Opt. Soc. Am.*, vol. 62, no. 1, pp. 55–59, 1972.
- [14.10] L. B. Lucy, “An iterative technique for the rectification of observed distributions,” *Astron. J.*, vol. 79, no. 6, pp. 745–754, 1974.
- [14.11] A. P. Dempster, N. M. Laird, and D. B. Rubin, “Maximum likelihood from incomplete data via the EM algorithm,” *J. Roy. Stat. Soc. B*, vol. 39, no. 1, pp. 1–38, 1977.
- [14.12] R. L. White, “Image restoration using the damped Richardson–Lucy method,” in *The Restoration of HST Images and Spectra II*, ed. R. J. Hanisch and R. L. White, Space Telescope Science Institute, 1994.
- [14.13] D. Kundur and D. Hatzinakos, “Blind image deconvolution,” *IEEE Signal Processing Magazine*, vol. 13, no. 3, pp. 43–64, 1996.
- [14.14] A. Levin, Y. Weiss, F. Durand, and W. T. Freeman, “Understanding blind deconvolution algorithms,” *IEEE Trans. Pattern Anal. Mach. Intell.*, vol. 33, no. 12, pp. 2354–2367, 2011.
- [14.15] P. C. Hansen, “Analysis of discrete ill-posed problems by means of the L-curve,” *SIAM Review*, vol. 34, no. 4, pp. 561–580, 1992.
- [14.16] G. H. Golub, M. Heath, and G. Wahba, “Generalized cross-validation as a method for choosing a good ridge parameter,” *Technometrics*, vol. 21, no. 2, pp. 215–223, 1979.
- [14.17] V. A. Morozov, *On the Solution of Functional Equations by the Method of Regularization*, Soviet Math. Dokl., 1966.
- [14.18] C. Stein, “Estimation of the mean of a multivariate normal distribution,” *The Annals of Statistics*, vol. 9, no. 6, pp. 1135–1151, 1981.

- [14.19] D. L. Donoho, “Compressed sensing,” *IEEE Trans. Information Theory*, vol. 52, no. 4, pp. 1289–1306, 2006.
- [14.20] E. J. Candès, J. Romberg, and T. Tao, “Robust uncertainty principles: Exact signal reconstruction from highly incomplete frequency information,” *IEEE Trans. Information Theory*, vol. 52, no. 2, pp. 489–509, 2006.
- [14.21] J. Kaipio and E. Somersalo, *Statistical and Computational Inverse Problems*, Springer, 2005.
- [14.22] A. M. Stuart, “Inverse problems: A Bayesian perspective,” *Acta Numerica*, vol. 19, pp. 451–559, 2010.
- [14.23] A. Gelman, J. B. Carlin, H. S. Stern, D. B. Dunson, A. Vehtari, and D. B. Rubin, *Bayesian Data Analysis* (3rd ed.), CRC Press, 2013.
- [14.24] N. Metropolis, A. W. Rosenbluth, M. N. Rosenbluth, A. H. Teller, and E. Teller, “Equation of state calculations by fast computing machines,” *J. Chem. Phys.*, vol. 21, no. 6, pp. 1087–1092, 1953.
- [14.25] W. K. Hastings, “Monte Carlo sampling methods using Markov chains and their applications,” *Biometrika*, vol. 57, no. 1, pp. 97–109, 1970.
- [14.26] R. M. Neal, “MCMC using Hamiltonian dynamics,” in *Handbook of Markov Chain Monte Carlo*, ed. S. Brooks et al., Chapman & Hall/CRC, 2011.
- [14.27] M. Raissi, P. Perdikaris, and G. E. Karniadakis, “Physics-informed neural networks: A deep learning framework for solving forward and inverse problems involving nonlinear partial differential equations,” *J. Comput. Phys.*, vol. 378, pp. 686–707, 2019.
- [14.28] J.-P. Tetienne *et al.*, “Quantum imaging of current flow in graphene,” *Nature Communications*, vol. 8, 15734, 2017.
- [14.29] D. A. Broadway *et al.*, “Quantum microscope for wide-field magnetic imaging,” *Nature Electronics*, vol. 3, pp. 502–507, 2020.
- [14.30] S. Li *et al.*, “Three-dimensional current-density reconstruction from vector magnetic-field imaging,” *Proceedings of the National Academy of Sciences*, vol. 119, e211 . . . , 2022.